IMPROVED TOTAL VARIATION RECONSTRUCTION METHODS FOR CARDIAC MAGNETIC RESONANCE IMAGING

by

Srikant Kamesh Iyer

A dissertation submitted to the faculty of
The University of Utah
in partial fulfillment of the requirements for the degree of

Doctor of Philosophy

Department of Electrical and Computing Engineering

The University of Utah

August 2017

The University of Utah Graduate School

STATEMENT OF DISSERTATION APPROVAL

The dissertation of **Srikant Kamesh Iyer**

has been approved by the following supervisory committee members:

Tolga Tasdizen	, Chair	**3/7/16** Date Approved
Edward Victor Rebok Di Bella	, Member	**3/7/16** Date Approved
Neal Patwari	, Member	**3/7/16** Date Approved
Ross Whitaker	, Member	**3/7/16** Date Approved
John Mathews	, Member	Date Approved

and by **Gianluca Lazzi** , Chair/Dean of

the Department/College/School of **Electrical and Computer Engineering**

and by David B. Kieda, Dean of The Graduate School.

ABSTRACT

Magnetic resonance imaging (MRI) is a popular imaging modality that allows for noninvasive detection of diseases without the use of ionizing radiation. Every imaging modality comes with its set of challenges and limitations. Since the rate at which data can be collected using an MRI scanner is relatively slow, data undersampling is often employed in order to accelerate acquisitions. This undersampling leads to artifacts in the reconstructed image due to the lack of sufficient data. In this dissertation, novel reconstruction techniques are developed to reconstruct high-quality and artifact-free images using a compressed sensing (CS) formulation. The reconstruction techniques are specifically designed and developed to handle the various challenges that occur in acquiring high-resolution myocardial perfusion images. Since the reconstruction of these images is often time consuming, techniques are developed to allow rapid reconstruction of images. Rapid reconstruction aids in the transition of CS techniques for myocardial perfusion MRI into a tool that is routinely used by clinicians.

This dissertation is dedicated to my family, especially to my mom and my dad, for their love and support throughout this journey.

CONTENTS

ACKNOWLEDGEMENTS

I would like to thank my advisors, Tolga Tasdizen and Edward DiBella, for their guidance and support. Thank you for introducing me to this fascinating world of medical image processing. I would also like to thank my committee members, Ross Whitaker, Neal Patwari, and John Mathews, for their valuable input. Special thanks to Lori Sather and Megan McAllister at the ECE department. Thanks for always being there to help me out.

I am thankful to the entire team at the Utah Center for Advanced Imaging Research (UCAIR) for providing a great research environment. I am also very thankful to Devavrat Likhite, Christopher Conlin, and Ganesh Adluru. Your presence made the years spent at UCAIR so much more memorable.

I would also like to acknowledge the role played by my family members; especially my mom, for motivating me to pursue a PhD, and my dad, for being a great role model--as a human being and as an engineer. A special thanks to my elder brother Omkar Iyer for his continued support throughout my life. His presence and moral support made graduate school less stressful.

I would like to thank my friends, Kausikram Krishnasayee, Vignesh Vaidyanathan, Avantika Vardhan, Prasanna Muralitharan, Amrish Kapoor, Uma Devi, Ramakrishna Sandeep, Shreyas Payal, Shashidhara Reddy, Josh Stott, and all my friends in Salt Lake City for making things memorable! Thanks to everyone who helped me along this journey.

I am also thankful to my school teachers. Thank you for being there to guide me during my most formative years. Nothing I have achieved would have been possible without your effort and guidance.

And finally, my sincere obeisance the Paramacharya of Kanchipuram, Sri Ganesha Hindu temple, Utah, and Sanatana Dharma foundation, New Jersey. I am certain that none of this would have been possible without divine intervention.

CHAPTER 1

INTRODUCTION

1.1 Background

Several medical imaging modalities have been developed since the 19th century to aid in the detection of diseases, including single-photon emission computed tomography (SPECT), positron emission tomography (PET), and X-ray. Compared to these imaging modalities, magnetic resonance imaging (MRI) is relatively safer as it does not use ionizing radiation to acquire the image, which, combined with the ability of MRI to better delineate between different soft tissues structures, has made MRI a popular imaging modality.

The protons present in various tissues of the body form the source of the signal in MRI. These spinning protons, which act as tiny magnets, are aligned in a magnetic resonance (MR) scanner by a strong external magnetic field to form a magnetization vector. This magnetization vector aligns along the direction of the external magnetic field in the z-direction. A radio-frequency (RF) pulse can then be applied to tip this magnetization vector to the x-y plane and a signal can be measured. Once the RF pulse is turned off, the signal begins to decay with a rate constant that is based on the physical property of the different tissues, including the T1 relaxation time and the T2 relaxation time. T1 relaxation or spin-lattice relaxation causes the protons to reorient back with the main magnetic field. The T2 relaxation or spin-spin relaxation causes the protons to dephase and magnetization in the transverse plane to decay. Using these two intrinsic relaxation parameters, the contrast of the image can be controlled to help delineate between different tissues. An MR pulse sequence is used to control the application of the RF pulse and the magnetic field gradients. These gradients are necessary to manipulate the magnetic spins and encoderelevant phase and frequency information.

Cardiovascular diseases are the leading cause of death worldwide and account for

over 17 million deaths per year. Over 86 million Americans suffer from some form of cardiovascular disease. Dynamic contrast-enhanced (DCE) MRI of the heart is a useful tool to detect and analyze cardiovascular diseases. A gadolinium (Gd)-based paramagnetic contrast agent is intravenously injected into the patient, and regions of the heart that receive the contrast agent have lower T1, depending on the concentration of the contrast agent at that location. When a T1-weighted sequence is used to acquire the data, regions that receive the contrast agent appear bright whereas regions that do not receive the contrast agent appear dark. This difference in contrast between different tissues can be used to detect diseases. For example, in DCE myocardial perfusion imaging, after the injection of the contrast agent, the contrast agent goes to the heart and then enters the myocardium via the coronary arteries. If the supply of blood to the different parts of the myocardium is uniform, the myocardium appears uniformly bright. If the blood supply to certain parts of the myocardium is reduced, say due to the presence of ischemia, such regions receive less contrast agent and hence appear relatively darker. This difference in contrast can be used by clinicians to visually differentiate between healthy tissue that is normally perfused and diseased tissue that may have reduced blood flow.

1.1.1 MRI image formation and Fourier space data

The MR scanner acquires data in Fourier space, also known as k-space. For a given field of view (FOV), when the k-space data is fully sampled, the image can be reconstructed by applying an inverse Fourier transform (IFT). Fig. 1.1 illustrates the relation between measured k-space and image space. The Fourier transform of a real function satisfies the Hermitian symmetry property. Since the magnetic field inside an MR scanner is not

perfectly uniform, the Hermitian symmetry property of Fourier space data is not satisfied by k-space data acquired in an MRI scanner. Hence the IFT of the measured k-space data yields a complex image. Fig. 1.1 shows the magnitude of the complex image that was formed by taking the IFT of the measured k-space data.

The data acquisition process in an MR scanner is inherently slow. The scanner uses a combination of linearly varying magnetic field gradients to acquire the different k-space lines. The data acquisition speed is usually constrained by the maximum gradient field strength and the slew rate. In imaging applications such as cardiac imaging, the imaging speed is of significant importance. Depending on the application, maintaining high spatial resolution and high temporal resolution becomes a tough balancing act, which has led to the development of techniques that undersample the acquired k-space data in order to accelerate the acquisition process.

In accordance with the Shannon/Nyquist theorem, acquisition of fewer data in k-space leads to aliasing artifacts in image space when a reconstruction technique such as IFT is used, a direct consequence of violating the Shannon/Nyquist sampling criterion. Compressed sensing (CS) aims to recover information from underdetermined linear systems. CS is a signal processing technique that is used to efficiently acquire and reconstruct signals from data that violate the traditionally used Shannon/Nyquist sampling criterion, making it an apt technique to improve MR image acquisition and reconstruction [1].

1.2 Principles of CS

The success of CS hinges upon two key principles being satisfied: incoherent random sampling and sparsity. The sampling pattern used to acquire the undersampled data must be such that the aliasing artifacts it produces are benign and noise-like. Fig. 1.2 shows two sampling patterns, Cartesian sampling and radial sampling, used to acquire undersampled k-space data of a Shepp-Logan phantom. When the k-space data are undersampled using a repetitive Cartesian sampling pattern, the IFT of the measured k-space leads to aliasing artifacts that appear as the original image folding back onto itself. When the radial sampling pattern is used to acquire the undersampled data, the artifacts appear like streaks across the image. Streaking artifacts are more benign compared to overlapped copies of the original image. The radial sampling pattern is more random than the repetitive Cartesian sampling pattern and hence produces more benign aliasing artifacts. Compared to the repetitive Cartesian undersampling pattern, radial sampling is considered a better undersampling pattern.

Sparsity relates to the number of nonzero values in a matrix. Most medical images are sparse either directly in the image domain or more commonly in some transformation domain. An example of transformation domain sparsity is shown in Fig. 1.3. The Shepp-Logan phantom is not directly sparse in the image domain, but the image gradients in the x and y directions are sparse. Hence for Shepp-Logan phantom, spatial gradients can be considered as sparsifying transforms or sparsifying operators. If some prior information is available about the transformation sparsity of the image we are trying to reconstruct, instead of merely using a linear reconstruction scheme like IFT, this information can be infused into the reconstruction algorithm to improve image quality.

The basic working principle of CS is to accelerate acquisition by using an incoherent random undersampling pattern, while reconstructing high-quality images by utilizing the property of transformation domain sparsity to remove aliasing artifacts and noise from the image.

1.2.1 Restricted isometry property

The notion of restricted isometry property of a matrix was introduced by Candes and Tao [2]. Consider a linear system of equation

$$\phi x = b . \tag{1.1}$$

Here b is a M-dimensional vector of measurements, ϕ is an M×N measurement matrix, and x is the N-dimensional signal. In order to find the sparsest signal consistent with the measurement, the following optimization problem has to be solved:

$$\min_x \|x\|_0, \text{ subject to } \phi x = b . \tag{1.2}$$

Solving (1.2) requires a combinatorial optimization and is very hard to solve [2]. The matrix ϕ is said to satisfy the restricted isometry property (RIP) if

$$(1-\delta_s)\|x\|_2^2 \le \|\phi x\|_2^2 \le (1+\delta_s)\|x\|_2^2 . \tag{1.3}$$

Here the isometry constant δ_s is the smallest number that satisfies (1.3). It has been shown in [2] that under certain conditions when the RIP is satisfied, the solution to (1.2) is equivalent to solving the following sparse optimization problem

$$\min_x \|x\|_1, \text{ subject to } \phi x = b . \tag{1.4}$$

Compared to (1.2), which is hard to solve, (1.4) can be minimized using standard linear programming techniques. The RIP property helps us use the L_1 norm to drive sparsity

instead of the L_0 norm.

1.3 CS image reconstruction formulation

Let *m* be the image we are trying to reconstruct from *d*, the measured k-space data. The relationship between *m* and *d* is given by

$$d = Em + \eta . \tag{1.5}$$

Here *E* is the forward operator or the encoding matrix, which includes the sampling pattern and the Fourier transform, and η is the noise in the data measurements. This type of formulation falls under the category called inverse problems. The aim is to estimate the image *m* given a set of k-space measurements *d*. Since we are dealing with undersampled data, the problem is ill posed as the solution to (1.5) is not unique because fewer k-space points have been measured compared to the dimension of the image we are trying to reconstruct. To tackle this problem, the number of possible solutions of (1.5) needs to be restricted by utilizing some prior information about the image *m*. Since the inclusion of the prior information restricts the number of possible solutions of (1.5), it is also called a constraint. The prior information that we have about the transformation sparsity of the image is applied to the reconstruction problem as a constraint in order to drive sparsity. If the constraint we are trying to apply is of the form $\phi(m)$, it can be combined with (1.5) and written as a Lagrangian equation

$$\underset{\min m}{C} = \left\| Em - d \right\|_2^2 + \lambda \phi(m) . \tag{1.6}$$

Here λ>0 is the Lagrange multiplier and the $\| \ \|_2$ is the L_2 norm. L_p norm of a vector $X=\{x_1,x_2,x_3 \ldots x_n\}$ can be defined as

$$\|X\|_p = (\sum_{i=1}^{n} |x_i|^p)^{1/p}. \quad (1.7)$$

The first term of (1.6), $\|Em - d\|_2^2$, is called the fidelity constraint and measures the closeness of the estimated solution *m* to the measured k-space data. The weight λ is used to control the amount of fidelity constraint and regularization that is applied to the reconstruction problem. It is also possible to derive (1.6) from a Bayesian framework. It can be shown that (1.6) is the maximum a posteriori (MAP) estimate of *m*, assuming η is independent and identically distributed (i.i.d.) additive white Gaussian noise (AWGN) and the prior density is of the form $\frac{1}{A}\exp(-\frac{\phi(m)}{B})$, where *A* and *B* are constants.

The choice of the constraint $\phi(m)$ depends on the properties of the data we are trying to reconstruct. For example, if the image *m* is smooth with no sharp discontinuities, we can use the L_2 norm of the gradient as a constraint to enforce this "smoothness" prior. This local smoothness prior is given by

$$\phi(m) = \|\nabla m\|_2^2. \quad (1.8)$$

Here ∇ is the spatial gradient operator. Applying (1.8) to the cost functional in (1.6), we get

$$\underset{\min m}{C} = \|Em - d\|_2^2 + \lambda\|\nabla m\|_2^2. \quad (1.9)$$

The solution *m* to (1.9) is given by the Euler-Lagrange equation

$$E^*(Em - d) - \lambda\Delta m = 0. \quad (1.10)$$

Here E^* is the complex conjugate of *E* and Δ is the Laplacian operator. For applications such as image denoising, there is a Fourier transform-based closed-form solution. For CS-type formulations in which the data are undersampled, a closed-form solution is not

available. Since the fidelity constraint and the sparsity constraint in (1.9) are purely convex, it is easy to use a gradient descent minimization scheme to reach a stable solution. The major drawback of using this smoothness prior is that the resultant image is often too blurred because the edges in the image get smoothed. Most natural images have sharp transitions such as edges and corners that correspond to the high-frequency components of the image. The use of H_1 regularization will cause a loss of the high-frequency information in the reconstructed image for our type of data, namely cardiac MR images, which are better characterized by a "piece-wise-constant with finite discontinuities" model.

The need for an edge-preserving sparsity constraint led to the development of total variation (TV), first introduced by Rudin, Osher, and Fatemi [3]. Since its inception, TV has quickly become a popular sparsity-inducing regularizer for several applications such image restoration [4], image denosing [5, 6], etc. The total variation (TV) constraint, also called the bounded variation (BV) regularization, is defined as

$$TV(m) = \left\| \nabla m \right\|_1 . \tag{1.11}$$

When the TV constraint is used as $\phi(m)$ in (1.6), the reconstruction model is popularly known as the Rudin, Osher, and Fatemi (ROF) model. The ROF model is thus defined as

$$\underset{\min m}{C} = \left\| Em - d \right\|_2^2 + \lambda \left\| \nabla m \right\|_1 . \tag{1.12}$$

Since the TV constraint uses an L_1 norm to penalize the gradients instead to the L_2 norm used in H_1 regularization, it is better suited to reconstruct images that conform to a piece-wise-constant model. Hence TV performs better at preserving sharp discontinuities as compared to H_1 regularization. The solution m to (1.12) is given by the Euler-Lagrange equation

$$E^{*}(Em-d)-\lambda\nabla.(\frac{\nabla m}{|\nabla m|})=0. \tag{1.13}$$

Minimizing the ROF model using traditional methods such as gradient descent leads to a slow rate of convergence due to the constraints on the step size used to implement gradient descent. The major drawback of minimizing the ROF model using gradient descent is that at locations in the image where the magnitude of the gradient is close to zero, (1.13) is not well defined due to the occurrence of singularities. One popular method to avoid this occurrence of singularities is to use a smoothed version of the L_1 norm by adding a small positive constant to the TV term as shown below.

$$TV(m)\approx\left\|\sqrt{\nabla m^{2}+\beta^{2}}\right\|_{1}. \tag{1.14}$$

Here β^2 is a positive constant. The properties of (1.14) depend on the value of β^2. If the value chosen in very small, (1.14) remains a good approximation of TV, but the rate of convergence with traditional methods such as gradient descent remains slow. If the value of β^2 is large, the approximation becomes poor and edges in the reconstructed image get smoothed. Usually the value of β^2 is chosen within the range 10^{-6}-10^{-9}. Even if β^2 is chosen in this range, the application of the smoothed version of TV can lead to several artifacts such as “staircase” artifacts [4] at edges, “checkerboard” artifacts at uniform regions in the image, and smoothing of fine texture in the image.

Better minimization techniques such as primal-dual algorithms [7] and variable substitution-based techniques such as Augmented Lagrangian (AL) [8, 9] and Split Bregman [6] have been developed to rapidly minimize TV. These techniques perform better at minimizing the ROF model as compared to a gradient descent-based implementation of the smoothed version of TV as defined in (1.14). AL and SB are

techniques that use auxiliary variables to make substitutions to enable the decoupling of the L_2 norm fidelity term and the L_1 norm TV term. The L_2 norm terms are usually faster to minimize as opposed to the L_1 norm term. Hence by using auxiliary variables-based substitution, the ROF model is split into several subproblems, each of which is easy to solve. The equivalence between AL and SB is well known [6]. In Chapter 5, a derivation is provided to better understand this equivalence between AL and SB. In addition, we provide a derivation to show that the "adding-noise-back" step [6] that is often used in SB formulations is also inherent to AL, although papers that use the AL formulation do not use this "adding-noise-back" step [9, 11]. The "adding-noise-back" step is a method to ensure that the sharp features such as edges or fine textures in the image, which may be lost due to the use of TV constraints, are added back to the reconstruction problem by updating the measured k-space data with the difference between the measured k-space data and the image estimate projected back into k-space using the encoding matrix E.

The focus of this dissertation is the development of TV-based reconstruction methods for cardiac MR applications such as gated multislice dynamic contrast enhanced (DCE) cardiac perfusion imaging, late gadolinium enhanced (LGE) imaging of the left atrium, and ungated DCE cardiac perfusion imaging. The focus is on developing TV methods that can reconstruct high-quality images from highly undersampled k-space data. The reconstruction methods are formulated to handle specific issues that arise due to the use of TV constraints such as edge smoothing, loss of contrast, and slow reconstruction speeds for each of these three data acquisition types.

Since the IFT of the measured k-space data gives a complex image, the TV-based reconstruction was implemented by applying the TV constraint on the real and imaginary

parts separately. The minimization of the cost functional gave a complex image as the solution. The images shown in this dissertation are the magnitudes of the complex images generated by the TV-based image reconstruction formulations.

1.4 Outline of dissertation

The dissertation is divided into six chapters, including the introduction and the conclusion. Chapter 2 describes a method to improve the spatio-temporal TV-based reconstruction technique [12] developed to reconstruct DCE cardiac perfusion images acquired using a 24-ray radial undersampling pattern. The method is specifically developed to tackle the problem of edge smoothing and loss of contrast in the reconstructed image by using edge maps to make the weight on spatial TV spatially varying while simultaneously using a gradient-matching function to improve the sharpness of edges. A data-driven reference image is generated to extract edge information and create the spatially varying edge map.

Chapter 3 presents a new accelerated acquisition and reconstruction technique for 3D LGE imaging of the left atrium. Data acquisition time is reduced by acquiring data accelerated using a variable density sampling pattern and acceleration factors R~3. 3D TV constraints are used to reconstruct images from the undersampled data. Since the use of traditional minimization techniques like gradient decent lead to slow rate to convergence, an SB-based implementation is developed to accelerate image reconstruction. The reconstruction time of this method is small and could allow for this technique to be used in a routine clinical setting. The method is tested on retrospectively undersampled preablation and postablation data to determine its efficacy. Another outcome of this study is to show

that for 3D LGE images, the “adding-noise-back” step for SB developed by Goldstein et al. [6] can be used to improve the reconstructed image quality beyond that achieved by the SB implementation, which does not use this “adding-noise-back” step.

Chapter 4 describes a new fast minimization technique for reconstructing multicoil DCE cardiac perfusion images. A combination of SB-based variable substitution and the iterative weighting technique developed for the fast iterative soft-thresholding algorithm (FISTA) [13] is used to accelerate image reconstruction. This novel minimization technique requires few variable substitutions and hence has low memory requirements. This is a key feature of this technique that makes it suitable for application on large datasets. This method is tested on gated and ungated cardiac perfusion images acquired using a golden angle sampling pattern. The results show that the multicoil TV reconstruction formulation minimized using the proposed variable substitution-based technique is able to generate high-quality reconstructions rapidly.

Chapter 5 provides a comparison of the SB and AL techniques and shows that the “adding-noise-back” step that is used in SB implementations can also be derived using AL.

Chapter 6, the concluding chapter, presents the contributions and provides recommendations for future work.

1.5 References

[1] M. Lustig, D. Donoho, and J. M. Pauly, "Sparse MRI: The application of compressed sensing for rapid MR imaging," *Magn. Resonance Med.*, vol. 58, pp. 1182-1195, Oct 2007.

[2] E. Candès and T. Tao , "Decoding by linear programming," *IEEE Trans. Inf. Theory*, vol. 51, pp. 4203–15, Feb 2005.

[3] L. I. Rudin, S. Osher, and E. Fatemi, "Nonlinear total variation based noise removal algorithms," *Physica D: Nonlinear Phenomena*, vol. 60, pp. 259-268, Nov 1992.

[4] S. Osher, M. Burger, D. Goldfarb, J. Xu, and W. Yin, "An iterative regularization method for total variation-based image restoration," *Multiscale Modeling & Simulation*, vol. 4, pp. 460-489, Jan 2005.

[5] A. Beck and M. Teboulle, "Fast gradient-based algorithms for constrained total variation image denoising and deblurring problems," *IEEE Trans. Image Process.*, vol. 18, pp. 2419-2434, Jun 2009.

[6] T. Goldstein and S. Osher, "The split Bregman method for L1-regularized problems," *SIAM J. Img. Sci.*, vol. 2, pp. 323-343, May 2009.

[7] T. F. Chan, G. H. Golub, and P. Mulet, "A nonlinear Primal-Dual method for Total Variation-Based Image Restoration," *SIAM J. Sci. Comput.*, vol. 20, pp. 1964-1977, May 1999.

[8] C. Wu and X. Tai, "Augmented Lagrangian method, dual methods, and split Bregman iteration for ROF, vectorial TV, and high order models," *SIAM J. Img. Sci.*, vol. 3, pp. 300-339, Jul 2010.

[9] S. Ramani and J. A. Fessler, "Parallel MR image reconstruction using augmented Lagrangian methods," *IEEE Trans. Med. Imag.*, vol. 30, pp. 694-706, Mar 2011.

[10] W. Yin, S. Osher, D. Goldfarb, and J. Darbon, "Bregman iterative algorithms for L1-minimization with applications to compressed sensing," *SIAM J. Img. Sci.*, vol. 1, pp. 143-168, Mar 2008.

[11] S. G. Lingala, E. DiBella, G. Adluru, C. McGann, and M. Jacob, "Accelerating free breathing myocardial perfusion MRI using multi coil radial k-t SLR," *Phys. Med. Biol.*, vol. 58, pp. 7309-7327, Oct 2013.

[12] G. Adluru, R. T. Whitaker, and E. V. DiBella, "Spatio-temporal constrained reconstruction of sparse dynamic contrast enhanced radial MRI data," *IEEE Int. Symp. Biomed. Imag.*, 2007, pp. 109-112.

[13] A. Beck and M. Teboulle, "A fast iterative shrinkage-thresholding algorithm for linear inverse problems," *SIAM J. Img. Sci.*, vol. 2, pp. 183-202, Mar 2009.

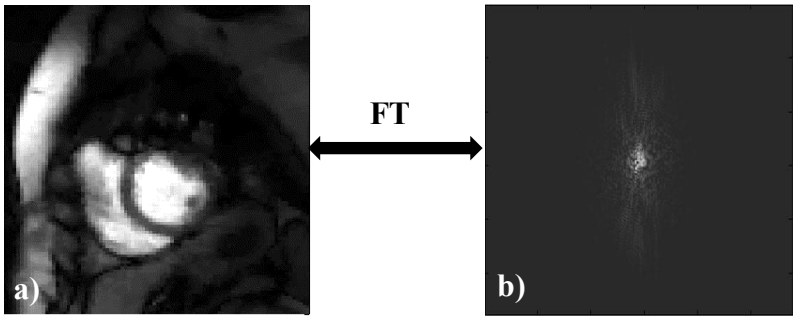

Fig. 1.1 The relationship between an image and the corresponding acquired k-space. The k-space data are the Fourier transform (FT) of the input image. Since kspace data do not satisfy Hermitian conjugate symmetry property, the IFT of the kspace data gives a complex image. (a) Magnitude of the complex image from the IFT of the kspace data and (b) magnitude of the complex kspace data are shown.

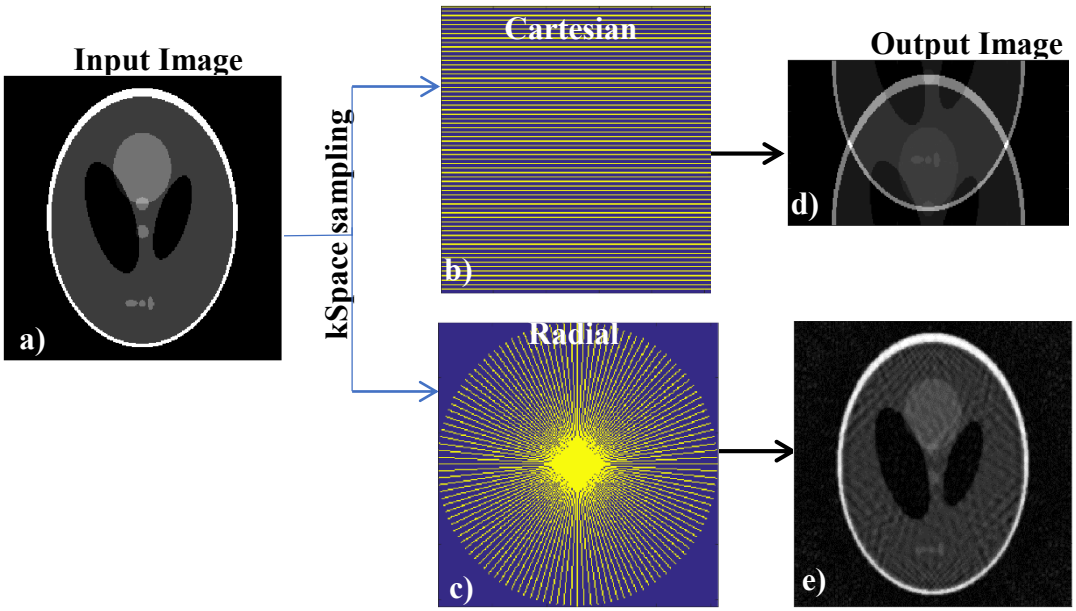

Fig. 1.2 The relationship between undersampling pattern and artifacts is shown using the (a) Shepp-Logan phantom. (b) Cartesian undersampling where the sampling pattern alternates between one line that is sampled and one line that is not sampled, (c) radial undersampling pattern, (d) overlapping artifacts due to undersampling with the Cartesian undersampling pattern shown in (b), and (e) streaking artifacts due to radial sampling. The radial undersampling pattern is more random compared to the repetitive Cartesian sampling pattern. Hence the streaking artifacts due to the radial undersampling pattern are more benign compared to the overlapping image artifact due to the repetitive Cartesian undersampling pattern.

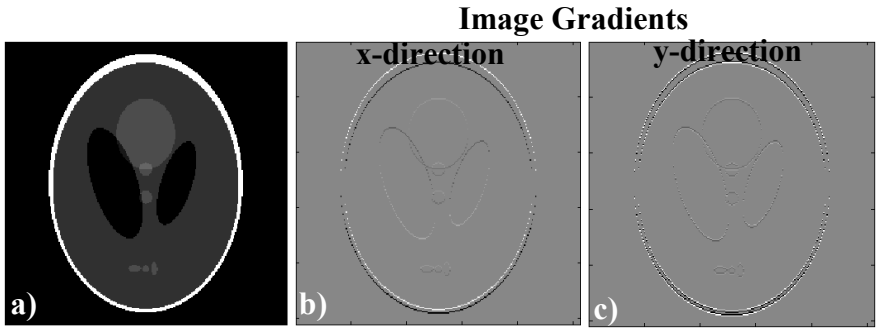

Fig. 1.3. An example of transform domain sparsity. (a) The Shepp-Logan phantom, (b) image gradient in the x-direction, and (c) image gradient in the y-direction. The Shepp-Logan phantom is not sparse in image space but its spatial gradients are sparse.

CHAPTER 2

EDGE-ENHANCED SPATIOTEMPORAL CONSTRAINED RECONSTRUCTION OF UNDERSAMPLED DYNAMIC CONTRAST-ENHANCED RADIAL MRI

This chapter is reprinted from "Edge enhanced spatiotemporal constrained reconstruction of undersampled dynamic contrast enhanced radial MRI" written by S. Kamesh Iyer, T. Tasdizen and E. DiBella and published in Magnetic Resonance Imaging, 30 (2012) 610–619. Reprinted with permission.

Available online at www.sciencedirect.com

SciVerse ScienceDirect

Magnetic Resonance Imaging 30 (2012) 610–619

MAGNETIC RESONANCE IMAGING

Edge-enhanced spatiotemporal constrained reconstruction of undersampled dynamic contrast-enhanced radial MRI

Srikant Kamesh Iyer[a,b,c], Tolga Tasdizen[a,b], Edward V.R. DiBella[c,d,*]

[a]Electrical and Computer Engineering Department, University of Utah, Salt Lake City, UT, USA
[b]SCI Institute, School of Computing, University of Utah, Salt Lake City, UT, USA
[c]UCAIR, Department of Radiology, University of Utah, Salt Lake City, UT, USA
[d]Department of Bioengineering, University of Utah, Salt Lake City, UT, USA

Received 3 March 2011; revised 15 July 2011; accepted 18 December 2011

Abstract

Dynamic contrast-enhanced magnetic resonance imaging (MRI) is a technique used to study and track contrast kinetics in an area of interest in the body over time. Reconstruction of images with high contrast and sharp edges from undersampled data is a challenge. While good results have been reported using a radial acquisition and a spatiotemporal constrained reconstruction (STCR) method, we propose improvements from using spatially adaptive weighting and an additional edge-based constraint. The new method uses intensity gradients from a sliding window reference image to improve the sharpness of edges in the reconstructed image. The method was tested on eight radial cardiac perfusion data sets with 24 rays and compared to the STCR method. The reconstructions showed that the new method, termed edge-enhanced spatiotemporal constrained reconstruction, was able to reconstruct images with sharper edges, and there were a 36%±13.7% increase in contrast-to-noise ratio and a 24%±11% increase in contrast near the edges when compared to STCR. The novelty of this paper is the combination of spatially adaptive weighting for spatial total variation (TV) constraint along with a gradient matching term to improve the sharpness of edges. The edge map from a reference image allows the reconstruction to trade-off between TV and edge enhancement, depending on the spatially varying weighting provided by the edge map.

Keywords: MRI; Reconstruction; Edge enhanced; Compressed sensing; Regularization; Cardiac perfusion

1. Introduction

In dynamic contrast-enhanced magnetic resonance imaging (DCE-MRI), a gadolinium (Gd)-based contrast agent is injected into the patient, and the T1 shortening effect of Gd makes regions that receive the contrast appear bright in the acquired T1-weighted images. To follow the dynamics of the contrast agent, high temporal and high spatial resolution is required. The MRI scanner requires a relatively large amount of time to acquire full data in k-space. Hence, simultaneous achievement of both high spatial resolution and high temporal resolution is challenging. When less data are acquired in k-space, a linear reconstruction scheme causes artifacts to appear in the image. The sampling pattern and its point spread function [1] determine the type of artifacts seen. In the case of radial acquisition, these artifacts appear as streaks across the image.

One major application of DCE-MRI is myocardial perfusion imaging. DCE cardiac perfusion imaging is an important clinical tool used to assess blood flow to the myocardium in order to detect coronary artery disease. Radial acquisition has been used in DCE cardiac perfusion imaging in part because radial acquisitions are relatively more robust to motion when compared to Cartesian acquisition. The reconstruction algorithm used to reconstruct the images from the undersampled k-space data must be able to reconstruct images with good contrast and sharp edges and must also be robust to some motion in the acquired data.

There have been many methods proposed to handle the problem of incomplete k-space data. Techniques like keyhole [2,3], reduced-encoding imaging with generalized-series reconstruction (RIGR) [4,5] and sliding window [6] have been used for reconstructing contrast-enhanced images

* Corresponding author.
E-mail address: ed@ucair.med.utah.edu (E.V.R. DiBella).

0730-725X/$ – see front matter © 2012 Elsevier Inc. All rights reserved.
doi:10.1016/j.mri.2011.12.021

and are relatively simple to implement. Most streaking artifacts in the image can be removed by these techniques, but images with high spatial and temporal resolution are often not achievable for high undersampling factors. Smaller structures and edges in the image often become blurred, and in the presence of respiratory motion, techniques like sliding window and keyhole perform poorly. This prevents their widespread use in cardiac perfusion imaging.

Cardiac images have high spatiotemporal correlations. Techniques like k-t Broad-use Linear Acquisition Speed-up Technique (BLAST) and k-t SENSitivity Encoding (SENSE) [7] exploit the spatiotemporal correlation by using dynamic training data. This helps in achieving high acceleration factors and also images with high resolution. But if there are inconsistencies between the training data and the reconstructed images, the method performs poorly. This reportedly makes k-t SENSE less robust to motion [8]. To overcome these limitations, the spatiotemporal domain-based unaliasing employing sensitivity encoding and adaptive regularization [9] algorithm used RIGR for its initial estimates. This reduces the problems associated with using a temporal average that is used in k-t BLAST and k-t SENSE and makes the method more robust to motion.

The idea of compressed sensing (CS) [1] aims to leverage sparsity constraints to reconstruct artifact-free images from relatively few k-space samples. k-t FOCal Underdetermined System Solver (FOCUSS) [10,11] and k-t SPARSE [12] are CS-based schemes that use the Fourier transform along the temporal domain as the sparsifying transform. These methods have been shown to be robust to motion [8]. CS-based methods can also be combined with parallel imaging techniques [8,13,14] to accelerate parallel imaging further.

Another way of exploiting the temporal correlations in DCE cardiac perfusion images in a CS framework is the use of temporal gradients as sparsifying constraints. Temporally constrained reconstruction [15,16] and, subsequently, a spatiotemporal constrained reconstruction (STCR) [17] have been shown to give good quality reconstructions of undersampled cardiac perfusion images with some respiratory motion using radial data with 24 rays. Here we propose to extend STCR in two ways. The first is to make the weight on the spatial constraint spatially varying. Such a spatially varying constraint was presented in Refs. [18–20]. In Ref. [18], a local noise measure was used to determine the spatial total variation (TV) constraint weight, with greater noise using higher weights. In Refs. [19,20], the scale of the objects in the image and the noise in the image were used to determine the weights of spatial TV constraint. In our method, the spatially varying weight is determined by edge strength. The second extension proposed here is to improve the sharpness of edges by adding an edge matching function based on a reference image. The new method is thus termed edge-enhanced spatiotemporal constrained reconstruction (EESTCR) [21].

2. Theory and method

2.1. Shortcomings of TV constraints

In Refs. [19,22], it was shown that TV denoising could lead to loss of contrast. In order to overcome the problem of loss of contrast due to TV, a spatially varying weight for TV was proposed by Strong and Chan in Ref. [20]. It was shown that a spatially varying weight for TV performs better at preserving contrast and also smaller features in the image. Two methods to make the weight spatially varying, namely, by using information about the size of different objects in the image, or by using information about noise in the image, were also developed. When reconstructing cardiac images, weight for TV should be large at uniform regions in the image to remove streaking artifacts and noise, while the weight should be small at edges to avoid smoothing and loss of contrast. Our method is motivated with this realization and proposes an automatic way to handle spatially varying weights by making use of information from a reference image.

2.2. EESTCR formulation

Aliasing artifacts occur in the image when Cartesian k-space is undersampled. When radial sampling is used, these artifacts appear as streaks in the image. However, any prior knowledge about the fully sampled image can be incorporated as constraints in a regularization framework to reduce or remove these artifacts. In EESTCR, the images are reconstructed by minimizing

$$C = \|Em - d\|_2^2 + \alpha_1 \sum_{i=1}^{N} \|\nabla_t m_i\|_1 + \alpha_2 \sum_{j=1}^{T} \|(1-\omega_j)\nabla m_j\|_1 + \alpha_3 \sum_{j=1}^{T} \|\omega_j^{1/2}\left(\nabla m_j - \nabla I_j^r\right)\|_2^2, \quad (1)$$

Where m represents the estimated complex image data and E is a matrix that models the physical imaging process. For MRI, E includes the k-space trajectory and also the Fourier transform operator. The fidelity term is given by $\|Em-d\|_2^2$, where $\|.\|_2$ represents the L_2 norm and d is the acquired sparse k-space data. The temporal regularization term is a TV in time penalty given by $\sum_{i=1}^{N} \|\nabla_t m_i\|_1$, where ∇_t is the temporal gradient operator, N is the total number of pixels in each time frame and m_i represents the time curve of pixel i. The spatial regularization term is a spatial TV [23,24] penalty given by $\sum_{j=1}^{T} \|\nabla m_j\|_1$, where $\|.\|_1$ represents the L_1 norm, T is the total number of time frames and ∇ represents the spatial gradient operator. The spatial TV constraint was implemented as shown in Ref. [16]. To improve the sharpness of the edges, we propose to add an edge constraint

given by $\sum_{j=1}^{T} ||\omega_j^{1/2}\left(\nabla m_j - \nabla I_j^r\right)||_2^2$, where I^r is the reference image and ω is a spatially varying weight defined as $\omega=1-\exp(-|(\nabla I^r)^2|/\lambda^2)$, in which λ is a constant. α_1, α_2 and α_3 are weights that control the amount of spatial TV regularization, temporal regularization and the gradient matching term, respectively. The reference image for each time frame is formed by combining three previous frames with the current time frame in a sliding window fashion. This allows each time frame to have its own reference image that follows the dynamics and motion of the acquired data.

The function ω(x,y,t) is used to form a spatially varying edge map of the strength of the edges in the reference image. It is assumed that the reference image does not suffer from artifacts due to incomplete k-space acquisition. The term (1−ω) is used to control the influence of the TV minimization at areas where the gradient of the reference image is large. At such points, the value of ω is close to 1, and hence, (1−ω) is almost zero. These low values of (1−ω) prevent the influence of TV minimization at sharp edges where only the edge matching function takes effect. This adaptive weighting leads to improvement of the sharpness of the edges by the edge constraint, and at the same time, the streaking and noise are removed by the spatial and temporal regularization terms.

An iterative gradient descent scheme with finite forward differences [25] was used to minimize the cost function. The dynamic series of images was updated at every iteration according to the following equation:

$$m_{n+1} = m_n - \eta C'(m_n); n = 1, 2, \ldots \quad (2)$$

Here n is the iteration number, η is the step size and C' is the Euler–Lagrange derivative of the cost functional with respect to m. The Euler–Lagrange derivative of the edge matching function is given by $\alpha_3\omega(\nabla^2 m - \nabla^2 I^r)$.

2.3. Data acquisition

The radial perfusion data were obtained using a Siemens Trio 3-T scanner with a phased array cardiac coil. A saturation recovery turbo flash sequence with repetition time/echo time ~2.5/1.4 ms, 12° flip angle and 8-mm slice thickness was used. The radial data had 24 rays in each time frame. A different start angle offset equal to an integer multiple of (180/96)° was used, and this was repeated every four frames so that a combination of four frames gave 96 unique equiangular rays. The method was tested on eight radial data sets acquired from six patients (four males and two females). Six data sets were acquired at rest, and two were acquired at stress. The contrast agent Gd-BOPTA, 0.03–0.04 mmol/kg, 5 cc/s, was used for rest and adenosine stress perfusion. The data were acquired with shallow breathing. The data were obtained using 9 to 15 receive coils of which 3–5 combined "coils" were reconstructed separately and 5 to 10 slices were acquired per study.

2.4. Reconstruction

First, the k-space data for each study were scaled to have the same range of intensities. The radial k-space samples were then interpolated onto a Cartesian grid for faster iterations as discussed in Ref. [16]. A reference frame for each reconstructed time frame was then created by combining the inverse Fourier transform (IFT) of the current time frame with the IFT of three frames before it in a sliding window fashion.

In order to determine the reconstruction parameters for EESTCR, a training data set was used. One of the eight patient data sets was chosen as the training data set, and it consisted of 8 slices and 53 time frames. To calculate the weight α_1, the L-curve technique was used. The weights α_2 and α_3 were set to zero. The elbow point in the L-curve corresponds to the best balance between the fidelity norm and temporal norm. We found that this elbow point was close to α_1=0.05 for each of the eight slices. An example is shown in Fig. (1). The weights α_2 and α_3 were then chosen empirically for the test data set. The regularization weights were chosen as α_1=0.05, α_2=0.005 and α_3=0.1. To choose the step size and the number of iterations for the reconstruction, the cost function was plotted against the number of iterations, and a combination of step size and number of iterations that led to a stable minimum was determined for the test data set. The step size for the gradient descent minimization was fixed at 0.05, and 150 iterations were performed to minimize the cost function C in Eq. (1). For the edge function ω, the value of λ was chosen as λ=0.045. The λ value that appeared to give the sharpest edges in the edge map ω was used.

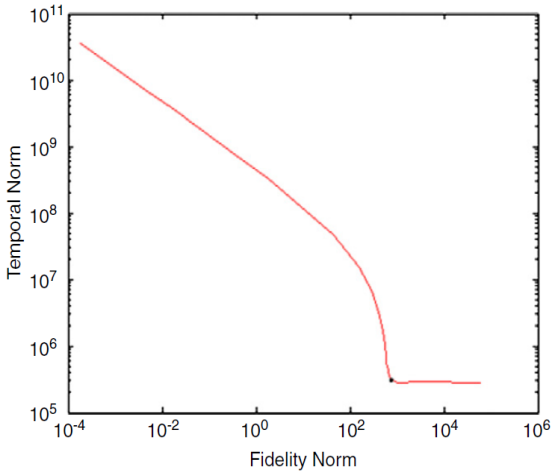

Fig. 1. An L-curve for one of the data sets used is shown. The elbow point in the log–log plot of the fidelity norm versus the temporal norm is α_1=0.05, shown by a dark point. Though the L-curve for only one slice is shown here, the elbow point for all of the slices was in a similar position. The α_1 values were continuously varied between 10^{-6} and 5.

Reconstructions were performed on data from each coil independently, and the images were combined using square root of sum of squares. The coils used to create the final images were chosen by visual inspection. This was done to avoid coils that produced heavy streaking artifacts.

2.5. Robustness of the method to small changes in the weights

To test the robustness of the method to small changes in the weights, the weights α_1, α_2 and α_3 were changed by ±20%, ±20% and ±50%, respectively, in different combinations of the three weights. Comparisons were made with images reconstructed using α_1=0.05, α_2=0.005 and α_3=0.1.

2.6. Comparison metrics

To compare the images reconstructed using EESTCR and STCR, we used a difference image. Plots of values in a line across the myocardium were also used to study the differences. The same line was plotted over time for both the methods, and a percentage difference between the two reconstruction methods was calculated. To study the robustness of EESTCR to motion, the method was applied to another set of three more patient data sets with large respiratory motion. The reconstructed images were compared with those of STCR for artifacts and false edges.

Contrast-to-noise ratio (CNR) and contrast were also calculated. Here CNR is given by the ratio $\frac{(MI_{Blood} - MI_{Myo})}{\sigma_{Bkg}}$, where MI_{Blood} is the mean intensity of a small region in the left ventricle (LV) blood pool, MI_{Myo} is the mean intensity of a small region in the myocardium and σ_{Bkg} is the standard deviation of a region in the background. Contrast is computed as $\frac{(MI_{Blood} - MI_{Myo})}{(MI_{Blood} + MI_{Myo})}$. CNR and contrast were calculated from a single time frame when the mean intensity in the LV blood pool was maximum and the regions were chosen close to the edge of the septal wall Fig. 2(A).

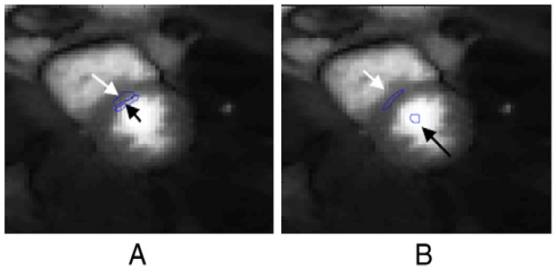

Fig. 2. Comparison of CNR and contrast for two choices of ROI. The regions are chosen (A) close to the edge in the myocardium and LV blood pool and (B) away from the edge. For the ROI shown in (A), CNR=88.12 and contrast=0.25 for EESTCR, and CNR=58.50 and contrast=0.18 for STCR. There are a 50.6% increase in CNR and a 39% increase in contrast. For the ROI shown in (B), no significant change in CNR and contrast was seen. CNR=250.2 and contrast=0.54 using EESTCR, and CNR=252 and contrast=0.53 using STCR.

3. Results

In general, the series of images reconstructed using EESTCR have better contrast and sharper edges than STCR results. The images in Figs. 3 and 4 show the improvement of edges in the LV and in the right ventricle (RV). The difference image shows that, in EESTCR, smoothing of edges is avoided and sharper edges are reconstructed. Also, the difference between the myocardium and blood pool is clearer in the EESTCR images when compared to STCR.

When trying to detect regions in the myocardium that have a perfusion defect, good contrast improves the ease with which such regions can be detected. This change in contrast in the region with less flow can be subtle in the reconstructed images. The images in Fig. 3 show that in the ischemic region in the myocardium [shown by the white arrow in Fig. 3(B) and (C)], the decrease in contrast in the myocardium is more visible in the image reconstructed using EESTCR. In the plot of the line in myocardium over time in Fig. 3(F), the difference is greatest at the edges of the LV myocardium. The spatial location of the line is shown in Fig. 3(A). The change in the line intensities across the myocardium plotted in Fig. 3(E) also shows that the valleys are lower and peaks are higher.

Sharper edges with EESTCR are shown for two time frames in Fig. 4. The difference between the myocardium and blood pool is more visible in images reconstructed using EESTCR. Also, finer structures like papillary muscles and the myocardium are better visualized in EESTCR. In STCR, finer structures can be mistaken for noise in the image, and these structures in the reconstructed image can be smoothed or removed. In EESTCR, by using a reference image to reduce the spatial TV weight at locations in the reconstructed image which are likely to have edges, this smoothing effect of TV is avoided.

The direction in which the intensities in the images reconstructed using EESTCR changed when compared to STCR is in a direction such as to increase the contrast in the image as opposed to STCR which will be in a direction such as to decrease the contrast in the image. In Fig. 5, we see that when gadolinium is present in the LV or RV, a 25% difference in the intensity between STCR and EESTCR was seen in the myocardium and the edges in LV and RV. The presence of gadolinium allowed improved detection of edges, and the edge map could be used by the gradient matching term to make the edges sharper. This difference was seen in a series of 10–15 time frames as shown in Fig. 5(D).

3.1. Robustness of the reconstruction to small changes in weights

We found that the method was robust to small changes in weights. A mean squared difference-based comparison of images reconstructed using the new set of weights that

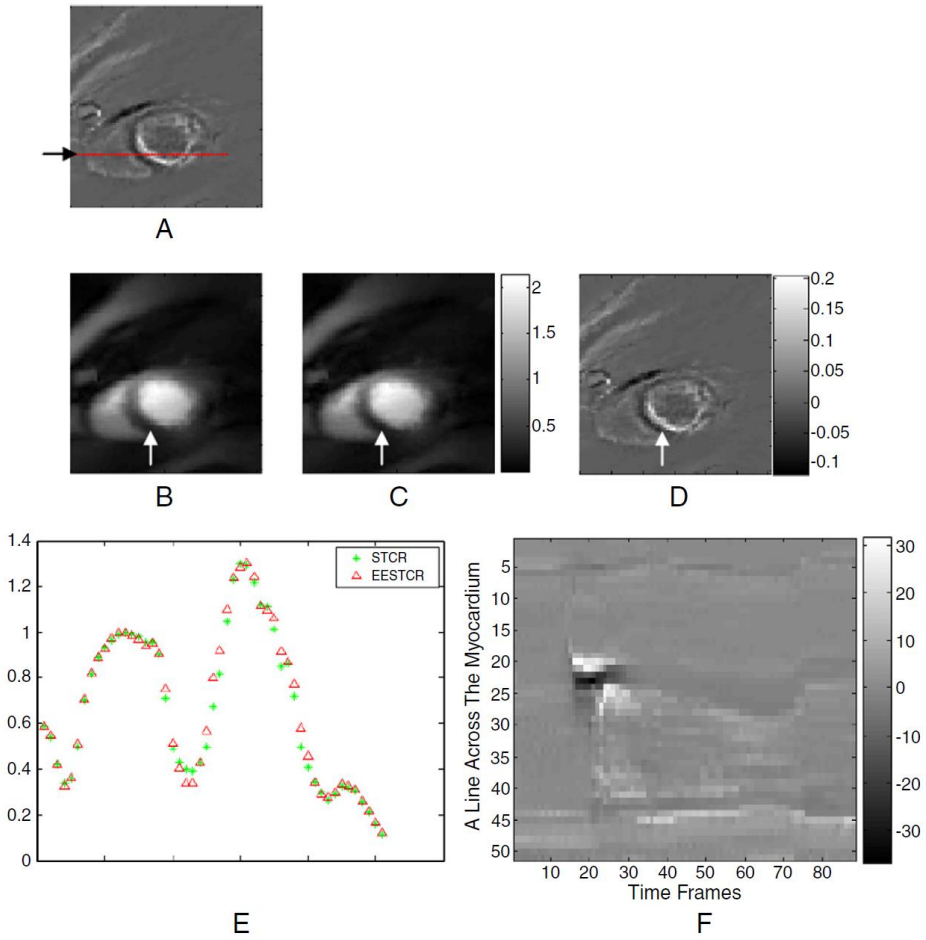

Fig. 3. The effect of using EESTCR when compared with STCR in a patient with ischemia. The images were reconstructed from radial data containing 24 rays. (A) Dotted line showing the spatial location of the plots. (B) Reconstructions using STCR, (C) reconstructions using EESTCR and (D) the difference image formed by taking the difference between EESTCR reconstruction in 1(C) and STCR reconstruction in 1(B). (E) Comparison of cross-sectional plot of a horizontal line across the myocardium as shown in 3(A). (F) A plot of the line across the myocardium in the difference image over time. The difference is shown in percentage scale.

had small perturbations and the standard set of weights showed that the differences were very small, usually in the order of 10^{-5} to 10^{-6}. An example is shown in Fig. 6. The maximum mean squared error seen in this data set was 7.6×10^{-6}.

3.2. Robustness to motion

There was respiratory motion present in the images shown in Figs. 3 and 4. Even in the presence of some motion, EESTCR was able to reconstruct images with sharper edges, showing that the method is robust to some motion. We found that, in some data sets, a good edge map could not be extracted because of a poor reference image. In such data sets, only slight or no improvement was seen in the sharpness of edges. However, a poor reference frame did not degrade the image quality, and the reconstructed image quality was very similar to STCR. The images in Fig. 7 show examples of a good edge map [Fig. 7(A)] and a poor edge map [Fig. 7(D)].

The performance of EESTCR on data sets with large motion and data sets with minimal motion is shown in Fig. 7. The edge map shown in Fig. 7(D) is blurred due to motion in the vertical direction. This causes the edges to appear broader in the edge map. Because the edges are blurred, the edge map detects edges at locations that may not correspond to edges in the reconstructed image. These blurred edges are usually less strong when compared to sharp edges, and hence, the weight on the edge matching function is no longer large. The method was used on three

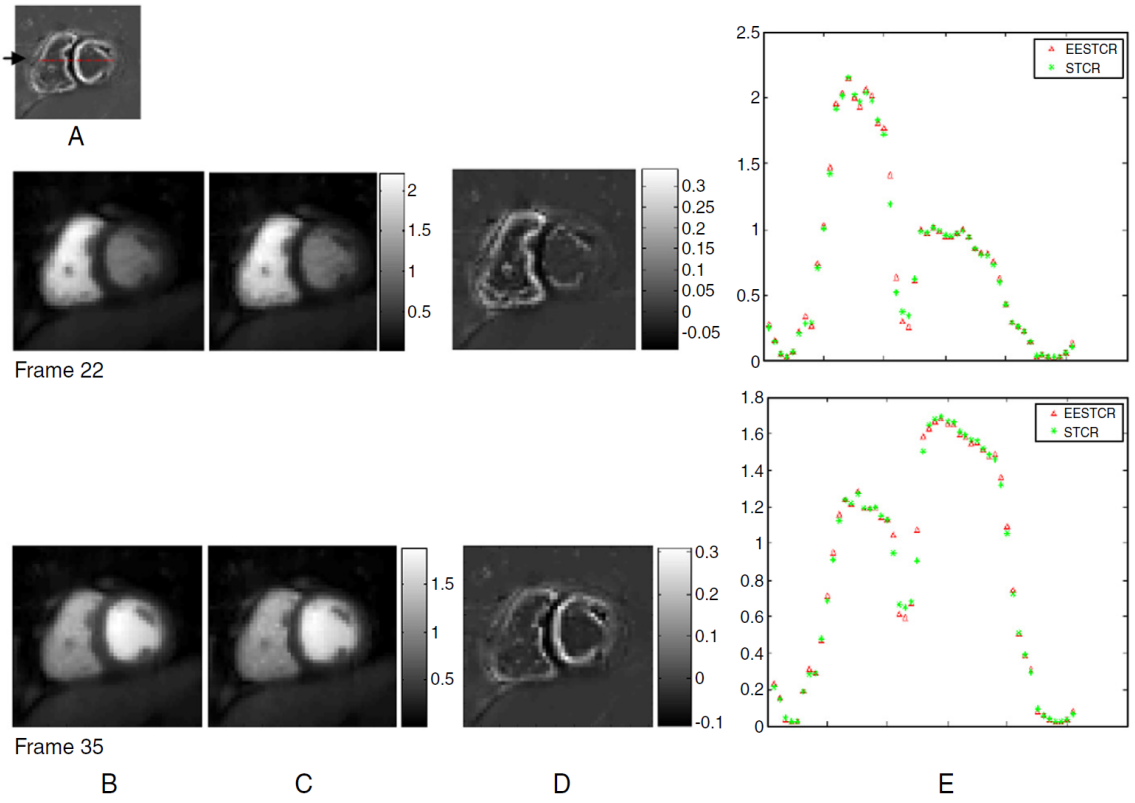

Fig. 4. Two time frames when Gd is present in the RV and LV, respectively. (A) Dotted line showing the location of the cross-sectional plot. (B) Images reconstructed using STCR, (C) images reconstructed using EESTCR and (D) the image difference between EESTCR (C) and STCR (B). (E) The cross-sectional plot of EESTCR and STCR across a horizontal line in the myocardium as shown by a dotted line in the image 4(A). The intensities at the lower edges have decreased, the intensities at the upper edge have increased, and better contrast is visible in EESTCR reconstructions.

data sets with large respiratory motion, and comparisons with STCR showed that no edge artifacts were added due to EESTCR. The images reconstructed using EESTCR matched those using STCR in image quality.

We found that if coils that had heavy streaking artifacts, such as from bright fat signal near the coil, were used for reconstruction, these streaking artifacts were added as false edges in the reconstructed image. This is because the weight added due to the edge map is no longer small and the presence of the artifacts in the acquired data at such locations would make the gradient matching term enhance the streaks. This problem can be mitigated by not choosing coils that have heavy streaking artifacts in them. The coils for the reconstructions were chosen by visual inspection.

3.3. Effect of EESTCR on segmentation

Manual registration and segmentation are often performed on the series of reconstructed images. This is done to extract time curves and flow reserves from the dynamic series of images. Contours have to be drawn around the myocardium to aid in the process of registration and segmentation. The presence of partial volume effect hinders this process. Also, signal from the blood pool should not be included with the myocardium during segmentation. The partial volume effect near the myocardium–blood pool interface is less in EESTCR when compared with STCR. This made the process of drawing contours easier. The contours with EESTCR images were often more conservative when compared with STCR, and the signal from the blood pool could be carefully avoided in the myocardium.

An example of the manual contours is shown in Fig. 8. The contours were first drawn on STCR [Fig. 8(A)] and overlaid on EESTCR [Fig. 8(B)]. The contours do not match the edges well, and signal from the blood pool in the LV and RV gets included with the myocardium in EESTCR. These regions are shown by the two black arrows in Fig. 8. A more conservative or narrow contour would have been drawn on

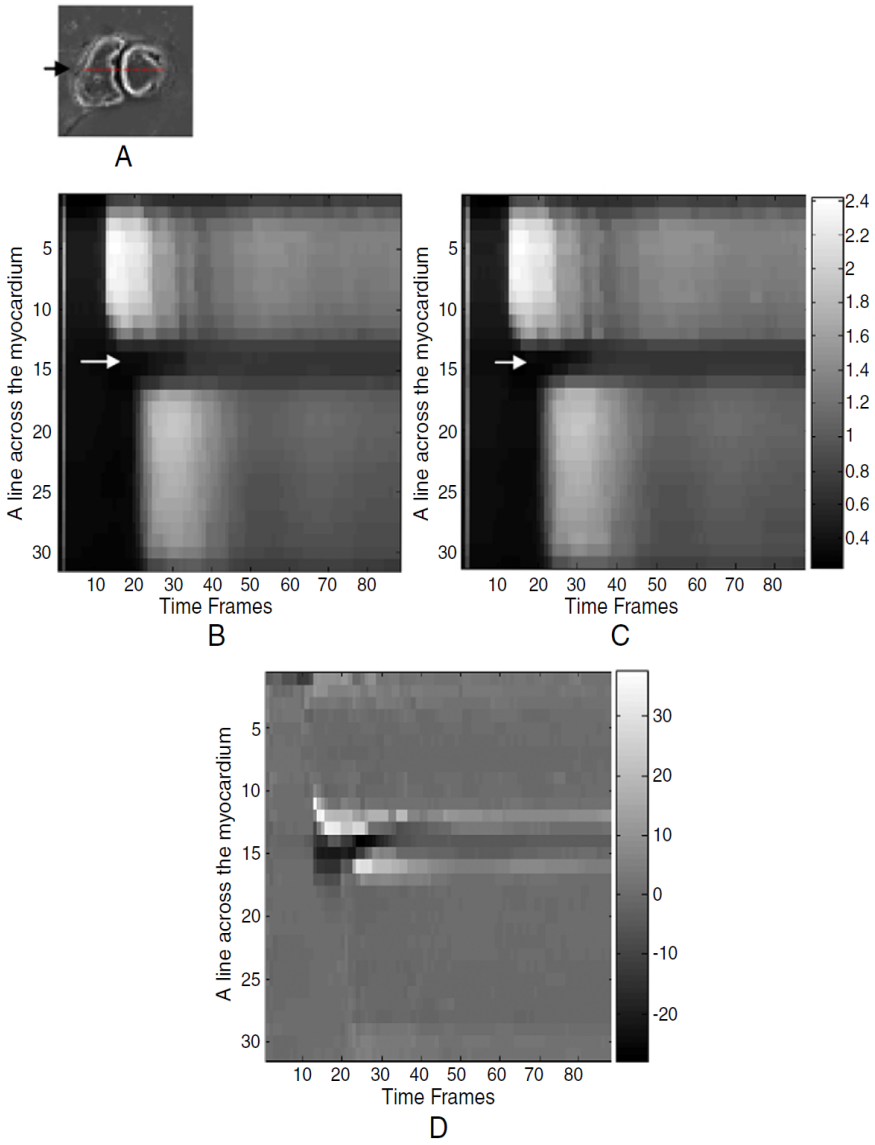

Fig. 5. The plot of a line across the myocardium over time. (A) The spatial location of the line. The plot of the line for image reconstructed using (B) STCR and (C) EESTCR is shown. (D) The percentage difference between (A) STCR and (B) EESTCR.

EESTCR image to avoid the blood pool signal from being included with the myocardium.

3.4. CNR and contrast

To calculate the CNR and contrast of images reconstructed using STCR and EESTCR, regions of interest were selected close to the edge of the myocardium and the LV blood pool, as shown in Fig. 2(A). There was on average a 36%±13.7% increase in the CNR and a 24%±11% increase in the contrast in images reconstructed using EESTCR when compared with STCR in five data sets. The standard deviations of the background for EESTCR and STCR reconstructed images were similar. When the standard deviation of a small region in the center of the blood pool was used instead of the standard deviation of the background, a similar percentage increase in CNR was seen.

For the example shown in Fig. 2(A), the CNR and contrast computed using EESTCR were CNR=88.12 and contrast=0.25. For STCR, CNR=58.5 and contrast=0.18. There were a 50.6% increase in CNR and a 39% increase in CR in this example. If the regions of interest were chosen well within the myocardium and blood pool, away from the edges [as shown in Fig. 2(B)], no significant change in CNR and contrast was seen. For the example shown in Fig. 2(B), CNR=250.2 and contrast=0.54 for EESTCR, and CNR=252

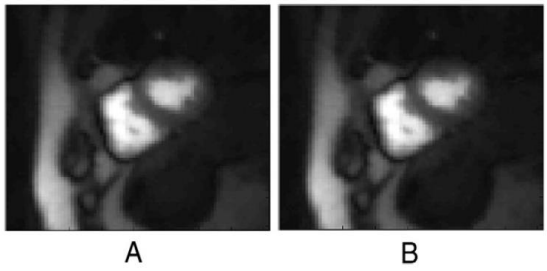

Fig. 6. Robustness of the reconstruction technique to small changes in the weights is shown. (A) Single coil image reconstructed using standard set of weights chosen: α_1=0.05, α_2=0.005 and α_3=0.1. (B) Image reconstructed using α_1=0.06, α_2=0.004 and α_3=0.05. The mean squared difference between (A) and (B) is 7.6×10^{-6}. This shows that the reconstruction algorithm is robust to small changes in the weights.

and contrast=0.53 for STCR. This shows that there is better contrast in EESTCR reconstructed images near the edges when compared to STCR. High contrast near the LV blood pool–myocardium boundary can help in the accurate detection of subendocardial ischemia.

4. Discussion

A new gradient matching term-based image reconstruction algorithm is presented. EESTCR is a data-driven approach to make the weight on the TV regularization spatially varying. Spatial gradients of a sliding window reference image that is generated from the undersampled data are used for this purpose. Unlike uniformly weighted TV, which can cause loss of contrast and smoothing of fine features in the image, in EESTCR, the spatially varying edge map makes the weight for TV spatially varying, and the smoothing effect of TV is avoided. The gradient matching term also enhances the edges in the reconstructed image by using an L_2 norm penalty with respect to the gradients of a reference image. The result of this edge enhancement is seen in the difference image and the cross sectional plots in Figs. 3 and 4. These show that EESTCR is better at handling trade-offs between smoothness of uniform regions and sharpness of edges. In data sets with large respiratory motion where only poor reference images with blurred edge maps could be extracted, the reconstructed image quality was comparable with STCR, and no false edge artifacts were added to the reconstructed image. This is because blurred edges usually tend to be less strong when compared with sharper edges. The presence of the temporal constraint at every pixel in the image also helps avoid these artifacts.

The temporal constraint is used to exploit the correlations in time of every pixel. As discussed in Ref. [16], the effect of the temporal constraint on the reconstructed image is more significant when compared to the spatial TV constraint. As a part of future work, spatially varying weights for the temporal constraint could be used so that different locations in the curve would be weighted differently. Any other information that can be extracted from the reference image, like the distribution of intensities, could also be used as a constraint in the reconstruction.

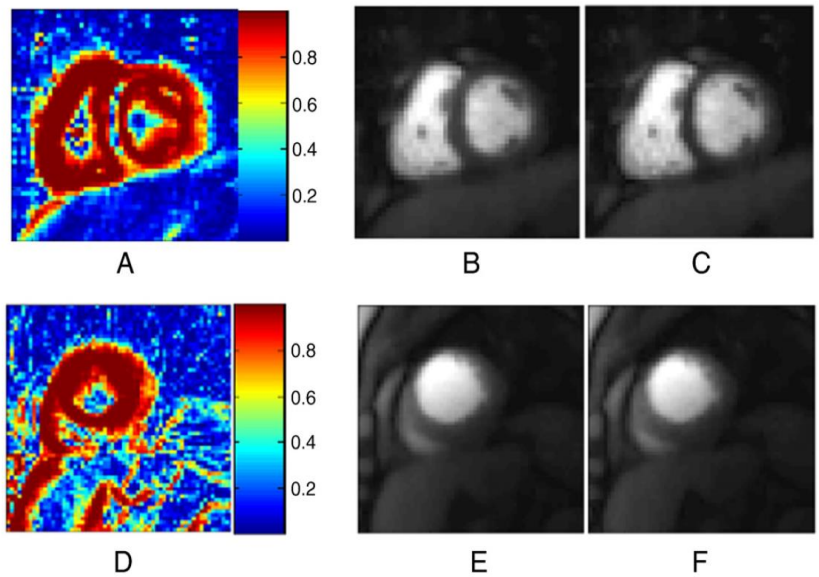

Fig. 7. The effect of reference images with different image qualities and their corresponding effect on the reconstructed image. (A) A good edge map. (B and C) The images reconstructed using STCR and EESTCR, respectively. The image reconstructed using EESTCR (C) has sharper edges as compared to STCR (B). The comparison is further shown in Figs. 4 and 5. (D–F) The effect of using a poor reference image, whose edges are blurred due to motion, as seen in 6(D). The reconstructions using EESTCR (F) are comparable with STCR (E). No false edges or artifacts have been added due to the blurred reference image.

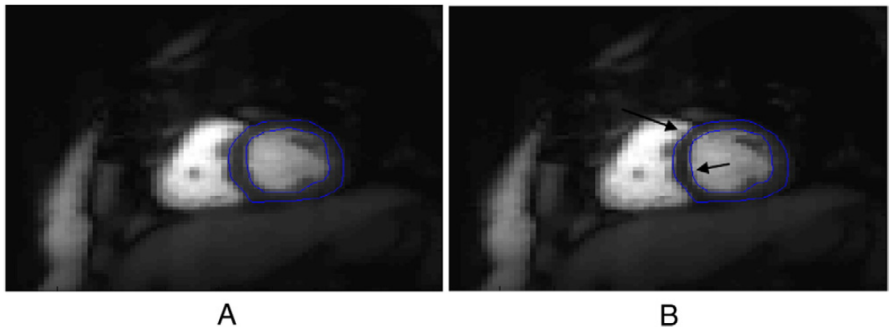

Fig. 8. The effect of EESTCR reconstructions on image segmentation is shown. The contours were drawn manually on STCR and overlaid on EESTCR. (A) Image reconstructed using STCR with its contour. (B) Image reconstructed using EESTCR with the contour from STCR overlaid on it. The contour from STCR is larger relative to EESTCR, and signal from the blood pool from LV and RV gets included with the myocardium. The regions where a more conservative contour would have been drawn in the EESTCR image are shown by the two arrows.

4.1. Loss of contrast due to TV minimization

TV minimization assumes that images are piecewise smooth or piecewise constant. This is often not true for medical images. Exact solutions for the change in intensity that is caused by TV were derived by Strong and Chan for simple images that have step edges like circles and rectangles and linearly varying edges [19,20,22]. It was shown that this change can be an increase or decrease of the original intensity and usually will be a direction that causes a decrease in contrast in the region. On a step edge, TV will cause the intensity of the lower edge to increase and the intensity of the higher edge to decrease, causing a decrease in contrast. With EESTCR, these increases of intensity at the lower edge and decrease of intensity at the higher edge have been avoided. In the difference image, the myocardial regions show negative intensity values, and the edges towards the LV and RV show positive values as shown in Figs. 3(D) and 4(D). The direction in which EESTCR causes a change in intensity at the edges matches the theoretical results predicted in Refs. [19,20,22].

4.2. Reference image and computational complexity

The reference images required for the spatially varying edge maps are extracted from the undersampled k-space data by combining multiple time frames in a sliding window fashion. As separate training data are not required to form the reference image, there is no additional acquisition time. Also, the formation of the reference image and the extraction of an edge map are computationally inexpensive. This edge map is similar to the one defined by Perona and Malik in Ref. [26] for denoising using anisotropic diffusion. But in anisotropic diffusion, a reference image-based method was not used for denoising the images.

The coils were reconstructed independently and then combined using the square root of sum of squares method. This helped reduce the reconstruction time by using the parallel processing toolbox in MATLAB to reconstruct the coils in parallel. On a Linux machine with 8 GB RAM and four processors, reconstruction of one slice with 66 time frames took 413 s and 457 s with STCR and EESTCR, respectively.

5. Conclusion

EESTCR is a promising technique to reconstruct DCE cardiac perfusion images from undersampled k-space data. The resulting images have sharper edges and higher contrast when compared to STCR. The method is robust to some motion. The method is also applicable to other DCE imaging techniques such as DCE tumor imaging of the brain or breast, where motion-related problems are less than with cardiac imaging. Small features like edges in the myocardium were better reconstructed in EESTCR, and there was improvement in contrast. Improvement in CNR and contrast was seen in the LV blood pool–myocardium region. The mean improvement was 36% for CNR and 24% for contrast compared to a similar method without use of the edge information.

References

[1] Donoho DL. Compressed sensing. IEEE Trans Inf Theory 2006;52:1289.
[2] Hu X. On the "keyhole" technique. J Magn Reson Imaging 1994;4:231.
[3] van Vaals JJ, Brummer ME, Dixon WT, Tuithof HH, Engels H, Nelson RC, et al. "Keyhole" method for accelerating imaging of contrast agent uptake. J Magn Reson Imaging 1993;3:671.
[4] Chandra S, Liang ZP, Webb A, Lee H, Morris HD, Lauterbur PC. Application of reduced-encoding imaging with generalized-series reconstruction (RIGR) in dynamic MR imaging. J Magn Reson Imaging 1996;6:783.
[5] Webb AG, Liang ZP, Magin RL, Lauterbur PC. Applications of reduced-encoding MR imaging with generalized-series reconstruction (RIGR). J Magn Reson Imaging 1993;3:925.
[6] Markl M, Hennig J. Phase contrast MRI with improved temporal resolution by view sharing: *k*-space related velocity mapping properties. Magn Reson Imaging 2001;19:669.
[7] Tsao J, Boesiger P, Pruessmann KP. k-t BLAST and k-t SENSE: dynamic MRI with high frame rate exploiting spatiotemporal correlations. Magn Reson Med 2003;50:1031.

[8] Otazo R, Kim D, Axel L, Sodickson DK. Combination of compressed sensing and parallel imaging for highly accelerated first-pass cardiac perfusion MRI. Magn Reson Med 2010;64:767.
[9] Xu D, King KF, Liang ZP. Improving k-t SENSE by adaptive regularization. Magn Reson Med 2007;57:918.
[10] Jung H, Park J, Yoo J, Ye JC. Radial k-t FOCUSS for high-resolution cardiac cine MRI. Magn Reson Med 2010;63:68.
[11] Jung H, Sung K, Nayak KS, Kim EY, Ye JC. k-t FOCUSS: a general compressed sensing framework for high resolution dynamic MRI. Magn Reson Med 2009;61:103.
[12] Lustig M, Santos JM, Donoho DL, Pauly JM. k-t SPARSE: High frame rate dynamic MRI exploiting spatio-temporal sparsity. In: Proceedings of the 13th Annual Meeting of ISMRM, Seattle, 2006. p. 2420.
[13] Ji JX, Zhao C, Lang T. Compressed sensing parallel magnetic resonance imaging. Conf Proc IEEE Eng Med Biol Soc 2008;2008:1671.
[14] Liang D, Liu B, Wang J, Ying L. Accelerating SENSE using compressed sensing. Magn Reson Med 2009;62:1574.
[15] Adluru G, Awate SP, Tasdizen T, Whitaker RT, DiBella EV. Temporally constrained reconstruction of dynamic cardiac perfusion MRI. Magn Reson Med 2007;57:1027.
[16] Adluru G, McGann C, Speier P, Kholmovski EG, Shaaban A, DiBella EV. Acquisition and reconstruction of undersampled radial data for myocardial perfusion magnetic resonance imaging. J Magn Reson Imaging 2009;29:466.
[17] Adluru G, Whitaker RT, DiBella EVR. Spatio-temporal constrained reconstruction of sparse dynamic contrast enhanced radial MRI data. Proc 4th IEEE International Symposium on Biomedical Imaging (ISBI); 2007.
[18] Huang F, Chen Y, Yin W, Lin W, Ye X, Guo W, et al. A rapid and robust numerical algorithm for sensitivity encoding with sparsity constraints: self-feeding sparse SENSE. Magn Reson Med 2010;64:1078.
[19] Strong D, Chan T. Edge and scale-dependent properties of total variation regularization. Inverse Problems 2003:19.
[20] Strong D, Chan T. Spatially and scale adaptive total variation based regularization and anisotropic diffusion in image processing. Diffusion in Image Processing, UCLA Math Department CAM Report; 1996.
[21] Kamesh Iyer S, DiBella EVR, Tasdizen T. Edge enhanced spatio-temporal constrained reconstruction of undersampled dynamic contrast enhanced radial MRI. Proc ISBI 2010:704.
[22] Strong D, Chan T. Exact solutions to total variation regularization problems. UCLA CAM Report; 1996.
[23] Candes E, Romberg J, Tao T. Robust uncertainty principles: exact signal reconstruction from highly incomplete frequency information. IEEE Trans Inf Theory 2006.
[24] Rudin LI, Osher S, Fatemi E. Nonlinear total variation based noise removal algorithms. Physica 1992;60:259.
[25] Karniadakis GEM, Kirby RM. Parallel scientific computing in C++ and MPI. New York: Cambridge University Press; 2003.
[26] Perona P, Malik J. Scale-space and edge detection using anisotropic diffusion. IEEE Trans Pattern Anal Mach Intell 1990;12:629.

CHAPTER 3

COMPRESSED SENSING FOR RAPID LATE GADOLINIUM ENHANCED IMAGING OF THE LEFT ATRIUM: A PRELIMINARY STUDY

This chapter is reprinted from "Compressed sensing for rapid late gadolinium enhanced imaging of the left atrium: A preliminary study" by S. Kamesh Iyer, T. Tasdizen, N. Burgon, E. Kholmovski, N. Marrouche, G. Adluru, E. DiBella and published in Journal of Magnetic Resonance Imaging, 2016 34: 846–854. Reprinted with permission.

Magnetic Resonance Imaging 34 (2016) 846–854

Contents lists available at ScienceDirect

Magnetic Resonance Imaging

journal homepage: www.mrijournal.com

Compressed sensing for rapid late gadolinium enhanced imaging of the left atrium: A preliminary study

Srikant Kamesh Iyer [a,b,d], Tolga Tasdizen [a,b], Nathan Burgon [c], Eugene Kholmovski [c,d], Nassir Marrouche [c], Ganesh Adluru [d], Edward DiBella [c,d,*]

[a] Electrical and Computer Engineering, University of Utah, UT, United States
[b] Scientific, Computational and Imaging Institute (SCI), University of Utah, UT, United States
[c] CARMA, Department of Internal Medicine, University of Utah, UT, United States
[d] UCAIR, Dept of Radiology, University of Utah, UT, United States

ARTICLE INFO

Article history:
Received 13 December 2014
Revised 19 February 2016
Accepted 3 March 2016
Available online xxxx

Keywords:
LGE imaging of the left atrium
Compressed sensing
Atrial fibrillation
MRI
Fast minimization

ABSTRACT

Current late gadolinium enhancement (LGE) imaging of left atrial (LA) scar or fibrosis is relatively slow and requires 5–15 min to acquire an undersampled (R = 1.7) 3D navigated dataset. The GeneRalized Autocalibrating Partially Parallel Acquisitions (GRAPPA) based parallel imaging method is the current clinical standard for accelerating 3D LGE imaging of the LA and permits an acceleration factor ~R = 1.7. Two compressed sensing (CS) methods have been developed to achieve higher acceleration factors: a patch based collaborative filtering technique tested with acceleration factor R ~ 3, and a technique that uses a 3D radial stack-of-stars acquisition pattern (R ~ 1.8) with a 3D total variation constraint. The long reconstruction time of these CS methods makes them unwieldy to use, especially the patch based collaborative filtering technique. In addition, the effect of CS techniques on the quantification of percentage of scar/fibrosis is not known.

We sought to develop a practical compressed sensing method for imaging the LA at high acceleration factors. In order to develop a clinically viable method with short reconstruction time, a Split Bregman (SB) reconstruction method with 3D total variation (TV) constraints was developed and implemented. The method was tested on 8 atrial fibrillation patients (4 pre-ablation and 4 post-ablation datasets). Blur metric, normalized mean squared error and peak signal to noise ratio were used as metrics to analyze the quality of the reconstructed images, Quantification of the extent of LGE was performed on the undersampled images and compared with the fully sampled images. Quantification of scar from post-ablation datasets and quantification of fibrosis from pre-ablation datasets showed that acceleration factors up to R ~ 3.5 gave good 3D LGE images of the LA wall, using a 3D TV constraint and constrained SB methods. This corresponds to reducing the scan time by half, compared to currently used GRAPPA methods. Reconstruction of 3D LGE images using the SB method was over 20 times faster than standard gradient descent methods.

1. Introduction

Atrial fibrillation (AF) affects over 7 million people in Europe and the US and is the most common cardiac arrhythmia. Acquisition of Late Gadolinium Enhancement (LGE) images of the left atrium (LA) is becoming a valuable tool for assessing the degree of fibrosis in the left atrium before and after treatment. Radio frequency (RF) ablation therapy is a promising procedure for treating AF and restoring sinus rhythm. Pre-ablation images have been used to detect fibrosis and are reported to be predictive of ablation outcome [1]. Post-ablation images can be used to detect the degree of ablation-induced scar in the LA wall [2,3]. While LGE images are very useful for non-invasive assessment of the LA wall, the image acquisition is relatively slow.

Current LGE acquisition methods for the LA use a 3D Cartesian inversion recovery pulse sequence with ECG gating and a respiratory navigator. In every heartbeat, after an inversion pulse has been applied, segments of 3D k-space are acquired while the heart is in the diastolic phase of the cardiac cycle and the diaphragm position is within a window. This acquisition process is inherently slow. The high spatial resolution required to assess the thin LA wall prolongs the acquisition further. Currently, the relatively long acquisition time of the 3D LGE sequence is a challenge to clinical workflow, particularly if an inversion time is chosen that does not give good results or the scan has to be repeated for other reasons such as patient motion.

* Corresponding author at: 729 Arapeen drive, Salt Lake City, UT, USA.
E-mail address: edward.dibella@hsc.utah.edu (E. DiBella).

http://dx.doi.org/10.1016/j.mri.2016.03.002
0730-725X/

Parallel imaging techniques like GRAPPA have been employed for faster acquisition, though reported acceleration factors for imaging the LA are less than R = 2 [2]. Advancements in compressed sensing (CS) [4,5] have made it possible to reconstruct good quality images from relatively few k-space samples by leveraging sparsity constraints. To the best of our knowledge, only two groups have looked at faster 3D LGE imaging. A 3D radial stack of stars acquisition with R ~ 1.8 (144 rays × 36 slab encodes) with a total variation (TV) constraint was used in [6], and a collaborative filtering method where the properties of similarity patches learned from the image were used as constraints with R = 3 [7,8]. Both methods are computationally intensive, especially the process of learning from patches. The reconstruction time for the patch-based method was reported as 98 min using a non-GPU based implementation [8]. These two CS reconstruction methods do not use rapid minimization techniques and hence suffer from long reconstruction times. In addition, the use of accelerated acquisitions could lead to loss of information about the amount of scar or fibrosis in the LA wall. The published CS techniques do not perform quantification of percentage of scar/fibrosis to study the effect of CS techniques on the quantification procedure.

The aim of this paper is to develop a rapid compressed sensing method and evaluate the acceleration factors that can be achieved, while maintaining good quality reconstructions and practical reconstruction times. Recently, several optimization methods such as the primal–dual algorithm [9], Split Bregman (SB) [10], and Augmented Lagrangian (AL) [11] have been developed, which can rapidly minimize compressed sensing objective functionals. Variable splitting methods like SB involve decoupling of the L_2 norm term from the L_1 norm term, which allows for rapid convergence of the minimization problem. Variable splitting techniques have been used to accelerate other compressed sensing methods for MRI. In [12], an AL based approach was developed for dynamic multicoil reconstruction with a Cartesian variable density sampling pattern. In [13], AL was used to accelerate sparse SENSE reconstructions where spatial TV and wavelets were used as sparsifying transform. Here we focus on the use of the Split Bregman (SB) approach to reconstruct LGE images of the LA with 3D TV, although the AL, dual algorithms and Split Bregman techniques are closely related, as shown in [11].

2. Method

2.1. Data acquisition

2.1.1. Patient data

To study the reconstruction method on human data, 8 fully sampled (4 post-ablation and 4 pre-ablation) datasets from atrial fibrillation patients were acquired with a Siemens 3 T Verio scanner. Acquisition parameters were TR = 3.8 ms, TE = 2.1 ms, TI = 300–400 ms, 36–40 slice encodings, a slice thickness of 2.5 mm and flip angle = 14° with 1.25 × 1.25 × 2.5 mm^3 resolution. The TI was chosen based on the nulling point of the myocardium. To reduce respiratory motion ghosting, the phase encoding direction was left–right. The size of the data matrix acquired from the scanner was ~320 × 320 × (36–40), transaxial slices. 32 channel phased array coils were used to acquire the data and a contrast agent dose of 0.1 mmol/kg of Gd-BOPTA was used. The images were acquired ~20 min after injection. A respiratory navigator (trailing) was used during the acquisition. It took ~10–15 min to acquire full k-space data.

2.2. Undersampling pattern

To produce undersampled data from the fully sampled data, a variable density sampling pattern was used, fully sampled along k_x, while directions k_y, k_z were undersampled using a bell shaped polynomial variable density distribution given by $P(y,z) = (1-r(k_y,k_z))^p$, where r is the normalized distance from the center of the sampling mask, given by $r(k_y,k_z) = \left(\frac{2}{\sqrt{n_1^2+n_2^2}}\right)\sqrt{k_y^2+k_z^2}$; $\frac{-n_1}{2} < k_y \le \frac{n_1}{2}$ and $\frac{-n_2}{2} < k_z \le \frac{n_2}{2}$. Here n_1 and n_2 are the sizes of the measured data matrix in the y and z directions, respectively. Points that are closer to the center have a higher probability of being sampled while points further away from the center have a lower probability of being sampled. The polynomial order (p) controls how densely the center of k-space is sampled. The higher the polynomial order, the smaller is the central k-space region being sampled.

2.3. Reconstruction

The standard compressed sensing approach can be written in a constrained form as:

$$\arg\min_m \|\phi m\|_1 \ \text{s.t} \|Em-k\|_2^2 < \sigma^2 \tag{1}$$

Where k is the measured k-space data, σ is the noise or artifact level in the measured k-space data, m is the (3D) image to be minimized, $\|\ \|_1$ is the L_1 norm, $\|\ \|_2$ is the L_2 norm, and E is the encoding matrix that includes the Fourier operator and an undersampling pattern. The symbol ϕ is a sparsity-promoting transform. In this paper, ϕ is the spatial gradient operator, which gives the total variation (TV) constraint.

Using the Bregman iterations technique, Eq. (1) can be reduced to a sequence of unconstrained optimization problems as shown in [14]

$$C_1 = \arg\min_m \|\phi m\|_1 + \frac{\mu}{2}\left\|Em-k^j\right\|_2^2 \tag{2}$$

$$k^{j+1} = k^j + k^0 - Em^{j+1} \tag{3}$$

Here μ is the weight that controls the tradeoff between sparsity of the image (the L_1 norm term) and closeness to the measured data (the L_2 norm term). Eq. (2) is a mixture of L_1 and L_2 norms, and using traditional methods like gradient descent for minimizing (2) has a slow rate of convergence. As shown in [10], (2) can be reduced to a series of unconstrained problems by introducing an intermediary variable d, such that $\phi m = d$ so that Eq. (2) can be written as:

$$\arg\min_{m,d,b} \|d\|_1 + \frac{\mu}{2}\left\|Em-k^j\right\|_2^2 + \frac{\lambda}{2}\|d-\phi m-b\|_2^2 \tag{4}$$

Where b comes from optimizing the Bregman distance [10]. The Bregman distance based on a convex function E between any two points u and v is given by, $D_E^p(u,v) = E(u) - E(v) - \langle p, u-v\rangle$, where p is the subgradient of E at v.

Using the Split Bregman formulation, fast convergence for L_1 regularized problems like those used in compressed sensing has been shown [10]. The measured k-space data k^0, which is updated as $k^{j+1} = k^j + k^0 - Em^{j+1}$ in Eq. (3), is equivalent to an "adding-noise-back" iterative step [15]. The derivation for this "adding noise back" step, based on Bregman distance and Bregman iterations is shown in [14]. By minimizing (4) and updating k as in (3), the constrained L_1 problem in (1) can be minimized in fewer iterations as compared to standard gradient descent based methods. Others have shown for denoising and deblurring applications that this type of "adding-noise-back" implementation produces images with less error and with edges that are sharper as compared to TV without the adding noise back step [15]. The SB method which includes "adding noise back" has been called the constrained version of SB [10] and the method that does not include "adding noise back" has been

called the unconstrained version of SB. The "adding noise back" step is a method to ensure that edges and fine textures that are lost due to TV regularization are included in the reconstruction. This adding noise back step can help improve the sharpness of edges in the reconstructed images.

The equation used to implement 3D TV based image reconstruction using SB is given as

$$\min_{m,dx,dy,dz,bx,by,bz} \left\| \sqrt{(dx)^2+(dy)^2+(dz)^2} \right\|_1 + \frac{\mu}{2}\left\|Em-k^j\right\|_2^2 + \frac{\lambda}{2}\|dx-\nabla_x m-bx\|_2^2 + \frac{\lambda}{2}\left\|dy-\nabla_y m-by\right\|_2^2 + \frac{\lambda}{2}\|dz-\nabla_z m-bz\|_2^2 \quad (5)$$

Here dx, dy and dz are the dummy variables introduced by the SB technique to enforce $dx=\nabla_x m$, $dy=\nabla_y m$ and $dz=\nabla_z m$, for the three directions x, y and z respectively. A minimum solution for m is found by alternatively minimizing m, dx, dy and dz. Algorithm 1 shows the steps followed to minimize the different variables. When trying to minimize m, the L_1 term (first term in Eq. (5)) that does not contain m is removed. By decoupling m from the L_1 norm term, fast convergence can be achieved. The update for m while dx, dy, and dz are held fixed is given as:

$$m^{i+1}=\min_m \frac{\mu}{2}\left\|Em-k^j\right\|_2^2 + \frac{\lambda}{2}\left\|dx^j-\nabla_x m-bx^j\right\|_2^2 + \frac{\lambda}{2}\left\|dy^j-\nabla_y m-by^j\right\|_2^2 + \frac{\lambda}{2}\left\|dz^j-\nabla_z m-bz^j\right\|_2^2 \quad (6)$$

The terms dx, dy and dz can then be minimized quickly by using the generalized shrinkage operator [10]. The minimization of the surrogate variables is performed in the inner loop of Algorithm 1 while the "adding noise back" step is performed in the outer loop of Algorithm 1.

2.4. Implementation of reconstruction

After undersampling the k-space data, coil compression with principal component analysis [16,17] was performed on the measured k-space data and the data were compressed into 4 virtual coils. Each coil was reconstructed separately and then the results combined with the square root of sum of squares. As discussed in [16,17], coil compression reduces the total number of coils required to reconstruct the image and hence reduces the reconstruction time. Experiments were performed to see how many virtual coils are necessary to reconstruct images without any loss of image quality due to coil compression. No loss of image quality was seen when 4 virtual coils were used to reconstruct the images. For some datasets it was possible to achieve good images with 3 virtual coils, but in order to maintain uniformity, 4 virtual coils were used to reconstruct all of the datasets.

The code was implemented in MATLAB. Parallel toolbox as well as Jacket 2.3.0 (AccelerEyes, Atlanta, GA) was used to run the reconstruction on GPU's. The code was run on an Nvidia Tesla C2070 with a total dedicated memory of 6 GB. The value of p was chosen as 1.6 and the weights for the reconstruction were chosen as $\lambda = 0.9$ and $\mu = 0.6$. These weights were chosen empirically to give the best visual image quality. Different weights were tested on the 8 datasets. Changing the weights by $\pm 50\%$ did not cause any major change in the visual quality of the image, though the convergence was slower when $\mu < 0.45$ was used. The set of weights chosen allowed for fast convergence of the reconstructed images.

2.5. Comparison metrics

(a) Visual inspection

The images were visually inspected for overall quality and also for sharpness and the ability to distinguish fine structures. The inverse Fourier transform (IFT) of the fully sampled data from each coil followed by square-root-of-sum-of-squares coil combination was used as "truth" to compare the reconstruction quality of images for different undersampling factors.

(b) Line profiles and difference images

To compare the sharpness of the LA wall in the reconstructed images with the fully sampled image, plots of intensities of a line across the LA were used. Image differences between the reconstructed image and fully sampled image were also computed to see if the residual difference image had any structures present or had a noise like pattern, especially in the LA.

(c) Normalized mean squared error and peak signal to noise ratio (PSNR)

The normalized mean squared error (NMSE) and PSNR give a sense of how different the reconstructed images are from the fully sampled image. Here NMSE was computed as $NMSE(m_{Full},m)=\|m_{Full}-m\|_2^2/\|m_{full}\|_2^2$, where m_{full} is the fully sampled image, m is the reconstructed image.

PSNR was computed as $PSNR = 20\log(\frac{Max_{m_{Full}}}{\sqrt{MSE}})$, where $Max_{m_{Full}}$ is the maximum intensity in the fully sampled image and mean squared error (MSE) is defined as $MSE(m_{Full},m)=\frac{1}{(Dim_X * Dim_Y * Dim_Z)}(\|m_{Full}-m\|_2^2)$, where Dim represents the dimension/size of the image in x, y and z directions.

(d) Blur metric:

The metrics described above use the fully sampled reference image in order to compute the metric. In contrast, the blur metric [18] is a reference image free metric that can be used to assess the quality of an image. The variation of an image with respect to a low pass filtered version of the same image can be used as an estimate for the amount of blurring in the image. After the low pass filtering process is performed, the difference is normalized to quantify the blur. An image with sharp edges would have a large variation with respect to the low pass filtered version while a smoother image would have smaller variation. The range of the blur metric is from 0 to 1, and a larger blur metric corresponds to a blurrier image.

(e) Quantification of the extent of LGE in the LA

The two CS techniques published for accelerating 3D LGE imaging do not perform quantification of the 3D LGE images to estimate the percentage of scar or percentage of fibrosis, which is part of the clinical procedure here and in some other locations. In order to study the effects of undersampling on the quantification procedure, the fully sampled images and the undersampled images were independently quantified and the results were compared.

The entire quantification procedure for the LGE images was performed by the Comprehensive Arrhythmia Research and Management (CARMA) center, University of Utah. The 3D LGE post-ablation images were used to calculate the percentage of scar present in the LA. The LA wall was first manually segmented. Manual segmentation was a laborious process for the ~40 slices. In order to make the process of quantification less laborious, comparisons were only made between the fully sampled image and images reconstructed using R = 3.5. Contours were manually drawn on the fully sampled image and separately on images reconstructed using R = 3.5 and then the percentage of scar quantified for the four post-ablation datasets. In order to estimate inter-observer variability, two of the four fully sampled post-ablation datasets were segmented by two users independently. An automated classification software [19] developed at the CARMA center, took the segmented images as input and calculated the percentage of scar in the post-ablation datasets. This automatic classification algorithm, based on clustering of voxels in the image, has been shown to

have good correlation with manual scar classification by expert observers [19].

To quantify the pre-ablation datasets, a semi-automated classification software [20] was used. The images were segmented manually as described above. After segmentation, classification of voxels was performed by thresholding the intensities in the LA wall. This thresholding was performed independently on each slice. A threshold was temporarily chosen by the semi-automated software by estimating the mean and standard deviation of non-fibrotic tissue. A final threshold was then manually chosen by the user at two to four standard deviations above the mean of the non-fibrotic tissue. Based on the extent of enhancement of the pre-ablation images, the patient was then classified into four groups [21]: stage I, stage II, stage III or stage IV. This type of classification can be used to help select appropriate medical strategies. It is important that undersampling the images does not lead to a different classification.

3. Results

3.1. Reconstruction of human datasets

Fig. 1 shows a comparison between a fully sampled image and undersampled versions of the data reconstructed with the unconstrained SB, which does not include "adding-noise-back", for a post-ablation dataset. When the "adding noise back" step is not used, blurring is visible in the reconstructed images. This is especially visible for higher acceleration factors of $R = 3.5$ and 4. In the difference image shown in Fig. 1 (e)–(g), fine texture is visible. This shows that sharp transitions in the reconstructed image have been smoothed. The blur metric and NMSE further show that the reconstructed images do not match the fully sampled image well. In addition, when the unconstrained SB method is used on the pre-ablation dataset, the loss of fine texture and smoothing of sharp transitions is even more evident (not shown). This is because in pre-ablation data, the relative enhancement in the LA wall is typically less than in post-ablation datasets.

Reconstruction of the post-ablation dataset shown in Fig. 1 using the constrained version of SB that uses "adding noise back" is shown in Fig. 2. The LA wall is better visualized and fine textures are better preserved in Fig. 2 than the images in Fig. 1. The lower NMSE and lower blur metric show that images in Fig. 2 match the truth better. For the post ablation datasets reconstructed using $R = 3.5$, the MSE and standard deviation on average were (8.9 ± 4.5).

To compare the unconstrained SB and constrained SB reconstructions further, intensities of a vertical line across the LA wall are plotted in Fig. 3 for the three reconstructions with undersampling factors $R = 3$, 3.5 and 4, to compare edge profiles with the truth. The location of this vertical line is shown by a thin red line in Fig. 3 (a). In Fig. 3 (b), the peaks of the curves that correspond to the constrained SB formulation match the truth well for the three acceleration factors $R = 3$, 3.5 and $R = 4$. The curves that correspond to the unconstrained SB formulation in Fig. 3 (c) have lower peaks as compared to the truth. This shows that the unconstrained SB formulation is not able to reconstruct the LA wall faithfully and there is a loss of contrast. This is further confirmed by the comparison of the PSNR for the three acceleration factors in Fig. 3 (d). For the unconstrained SB formulation, where the "adding noise back step" is not used, the PSNR is lower than the constrained SB formulation for all three acceleration factors.

The reconstructions from $R = 3$, 3.5 and 4 using the constrained SB approach for a pre-ablation dataset are shown in Fig. 4. The images show that the reconstructed images match the fully sampled image well. At undersampling factors of $R = 4$ some minimal smoothing is seen, though the enhancement in the LA wall is still visible. For the pre-ablation datasets reconstructed using $R = 3.5$, the MSE and standard deviation on average were (11.7 ± 5.5).

The difference images in Figs. 2 and 4 show few fine structures, as the reconstructions closely matched the truth. The blur metrics calculated on the reconstructed images for the 3 acceleration factors are close to the blur metric calculated on fully sampled image. This shows that the sharpness of the edges in the reconstructed images matched the sharpness of the fully sampled image well and that there was not much increase in smoothing beyond that present in the fully sampled image.

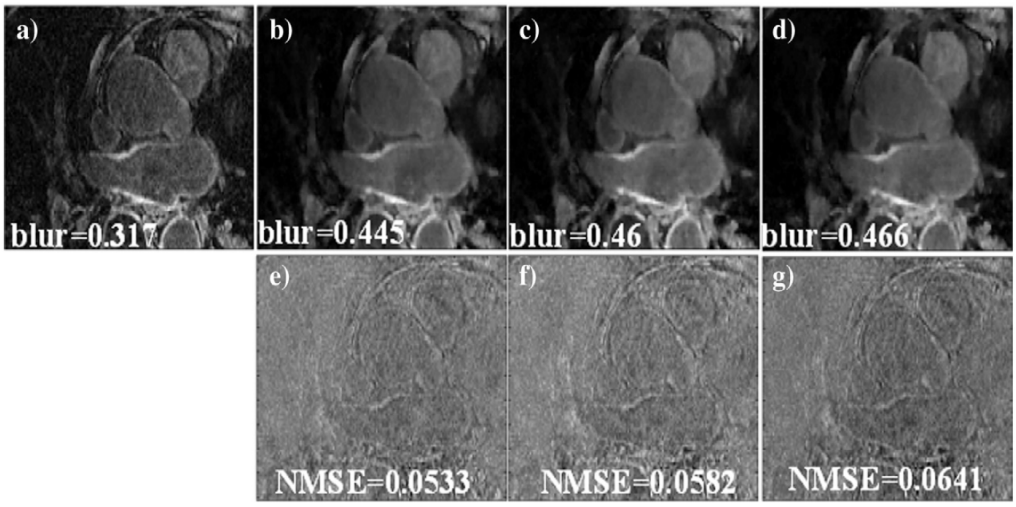

Fig. 1. (**a**) Cropped LA region in one slice from a fully sampled image. (**b**), (**c**) and (**d**) Reconstructions using the unconstrained SB method with no "adding noise back" term for R= 3, R=3.5, and R=4 respectively (only using Eq. (6)). The blur metric for the truth and the reconstructed images are reported along with the images. (**e**), (**f**) and (**g**) Difference image between the truth and the images reconstructed in (b), (c) and (d) respectively. The MSD of the individual slice is shown along with the difference image. Blurring of the LA wall was visible in these reconstructions that use the unconstrained SB method.

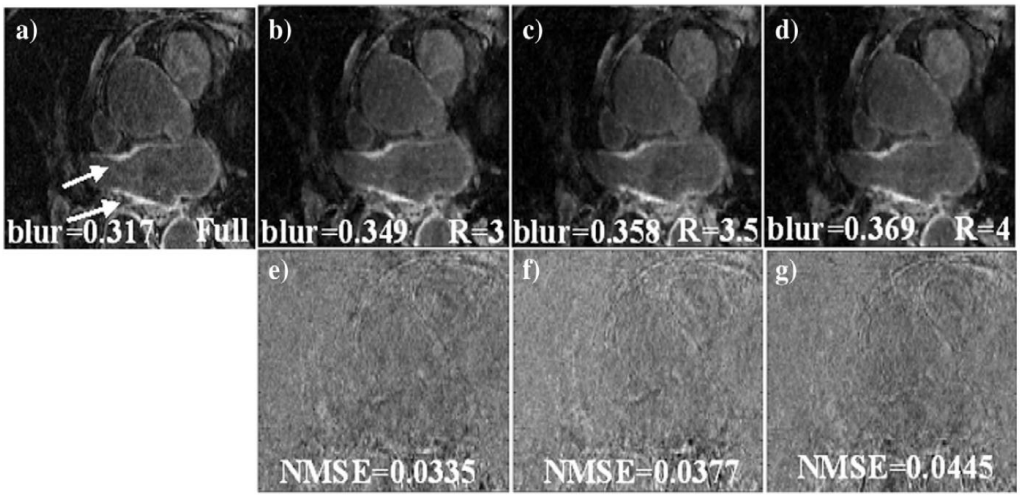

Fig. 2. (**a**) Cropped LA region in one slice from a fully sampled image; the arrows point to the enhancement in the LA wall. (**b**), (**c**) and (**d**) Reconstruction using the proposed method with "adding noise back" for R = 3, R = 3.5 and R = 4 respectively (using Eqs. (6) and (3)). The blur metric for the truth and the reconstructed images is reported along with the images. (**e**), (**f**) and (**g**) Difference image between the truth and the images reconstructed in (b), (c) and (d) respectively. The MSE of the individual slice is shown along with the difference image.

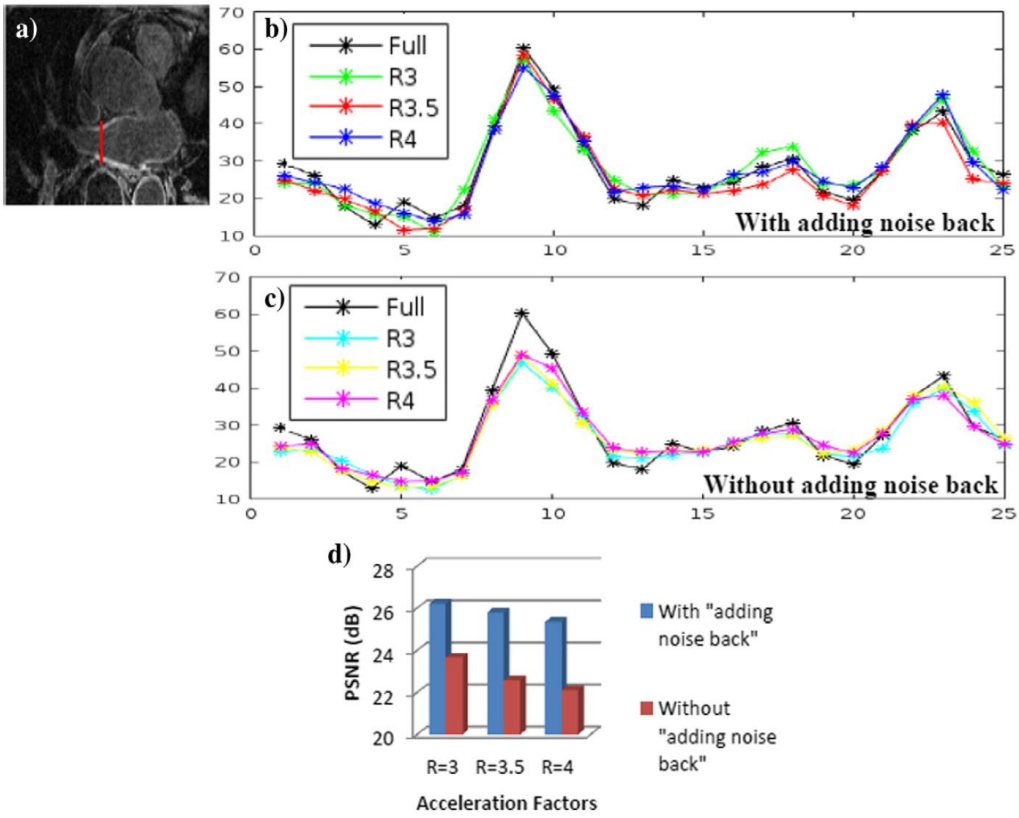

Fig. 3. **A** comparison of the constrained SB formulation (with "adding noise back" step) with the unconstrained SB formulation (without "adding noise back" step). (**b**) Plot of a line across of the LA wall for the images in Fig. 2 that correspond to the constrained SB formulation; the location is shown by the thin red vertical line in (**a**). For all of the three acceleration factors, the peaks of the curves from the reconstructed images match the truth. (**c**) Plot of a line across the LA wall for the images in Fig. 1 that correspond to the unconstrained SB formulation. For all of the three acceleration factors, the peaks of the curves from the reconstructed images are lower than the truth. (**d**) The comparison of PSNR for the unconstrained SB images in Fig. 1 and constrained SB images in Fig. 2. The PSNR with constrained SB formulation is higher than the unconstrained SB formulation for all three acceleration factors. These results show that the constrained SB formulation that uses the "adding noise back" step can reconstruct images with better contrast and sharper edges.

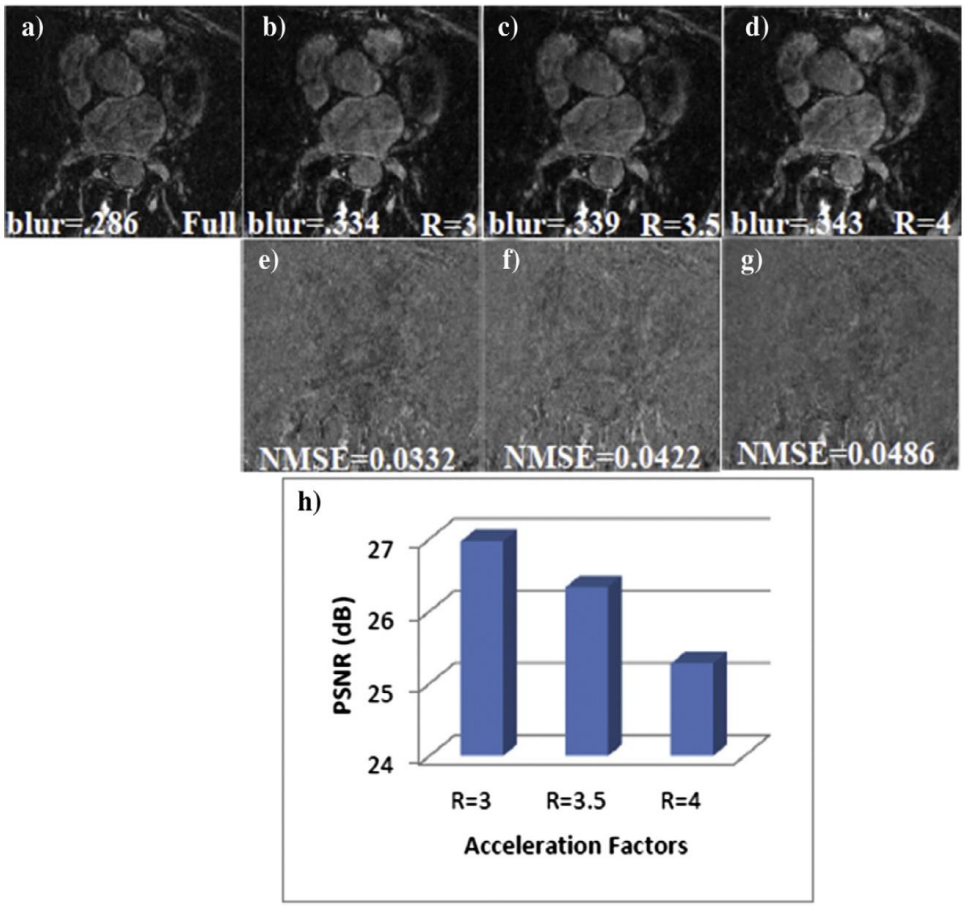

Fig. 4. (**a**) A slice from a fully sampled image from a pre-ablation dataset. (**b**), (**c**) and (**d**) Reconstruction using the proposed constrained SB method for R = 3, R = 3.5 and R = 4 respectively. The blur metric for the truth and the reconstructed images is reported along with the images. (**e**), (**f**) and (**g**) Difference image between the truth and the images reconstructed in (b), (c) and (d) respectively. (**h**) Bar chart comparing the PSNR of images reconstructed using R = 3, R = 3.5 and R = 4.

3.2. Quantification of enhancement

3.2.1. Quantification of ablation on post-ablation datasets

3.2.1.1. Study of inter-user variability. The result of the two fully sampled post-ablation images quantified by two independent users is shown in Table 1. The difference between the two observers was ~2.5% on average. While the number of datasets used was small, the inter-user variability seen here was similar to the inter-user and intra-user variability of about ±3% reported in [1], where a much larger number of datasets was used. When 3D rendering [2] of the segmented images was performed, it was seen that there was a small change in shape, location and degree of scarring detected by the two users. This gave an estimate of the inter-user variability in both the estimation of percentage of scar and locations where scarred tissue is detected.

Table 1
Comparison of percentage fibrosis calculated from the fully sampled images for two post-ablation datasets which were independently segmented by two users. The percentage fibrosis calculated by the two users matched well. The small variation in the percentage of scar calculated by the two users is mostly due to the intra-user variability in the segmentation process.

User 1	User 2
15.9%	18.5%
9.8%	12.2%

3.2.1.2. Quantification of percentage of scar from R = 3.5 images. A comparison of quantification of the fully sampled image and the images reconstructed using R = 3.5 for the four post-ablation datasets is shown in Fig. 5. It was found that the difference between the values calculated was ~2% on average. When 3D rendering of the fully sampled image and the image reconstructed using R = 3.5 was performed after segmentation, the percentage scarring and location of scar estimated from the fully sampled images and the R = 3.5 images were similar.

3.2.2. Quantification of pre-ablation data

The percent enhancement estimated by the quantification procedure using R = 3.5 closely matched those estimated from the fully sampled image for the four pre-ablation datasets. For all of the four datasets, the classification of the patient based on the quantification of enhancement was the same for the fully sampled image and for R = 3.5 images. The results for the four datasets are shown in Table 2. When 3D rendering of the segmented images was performed, the location of

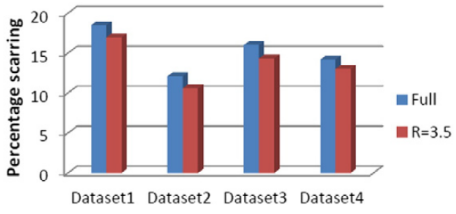

Fig. 5. The comparison of percentage scarring calculated from the fully sampled image and the images reconstructed from R = 3.5. The difference between the values calculated from the fully sampled image and the images reconstructed from R = 3.5 is within the expected inter and intra-user variability.

enhancement and the percentage fibrosis detected matched well between the fully sampled image and R = 3.5 images.

3.3. Convergence and reconstruction time

For all of the datasets the number of iterations for the inner loop in Algorithm 1 was fixed to 10 iterations. It was necessary to perform the outer loop for updating k only 4–8 times to reach convergence, assuming a convergence criterion of $\frac{\|m^{k+1}-m^{k}\|}{\|m^{k+1}\|} \leq 5 \times 10^{-3}$. Similar findings were reported in [10]. To be conservative, 10 iterations were used for both the inner and outer loops; a total of 100 iterations were performed to reconstruct each dataset. The average reconstruction time for the SB method to reconstruct a 3D dataset with 44 slices was 8 s on a Linux platform, 16 CPU cores (Intel Xeon CPU E5620 @ 2.40 GHz), 2 GPU cards (NVIDIA Tesla C2070) and 96 GB RAM. This was much faster compared with the gradient descent method, which on average took about 170 s to reconstruct the images on the same platform. This corresponds to a speedup of over 20 using SB.

4. Discussion

We developed a rapid SB 3D total variation reconstruction method for fast acquisition of 3D LGE images of the LA that outperformed gradient descent based methods. The gradient descent based implementation used a smooth approximation of the L_1 norm by adding a small positive constant to avoid singularities that occur when the magnitude of the gradient is close to zero. This smooth approximation caused smoothing of edges in the reconstructed image. When the SB method without the "adding noise back" step was considered, it performed slightly better at edge locations compared to the gradient descent based implementation of the same minimization problem, though the overall image quality was similar. The use of soft thresholding to minimize the L_1 norm in SB based implementations performs better than the smooth approximation used while implementing the L_1 norm in gradient descent based implementation. When compared to the unconstrained SB method that does not use the "adding noise back" step, the constrained SB method with "adding noise back" helped reconstruct good quality images that matched the fully sampled image better.

Table 2
Comparison of percentage fibrosis calculated from the fully sampled image and the image reconstructed from R = 3.5 for four pre-ablation datasets. The percentage fibrosis calculated from the fully sample data matches that calculated from R = 3.5 well. The classification of patients based on the percentage fibrosis calculated from R = 3.5 matches the classification from the fully sampled data.

	Full Image	Classification	R = 3.5	Classification
Dataset Pre-1	14.3%	Utah II	17.9%	Utah II
Dataset Pre-2	7.2%	Utah I	6.2%	Utah I
Dataset Pre-3	8.4%	Utah I	6.4%	Utah I
Dataset Pre-4	15.5%	Utah II	15.4%	Utah II

The constrained SB method that uses the "adding noise back" step has an equivalent AL version that can be shown to also have this "adding noise back" step; the near equivalence between SB and AL is shown in [11,14]. "Noise" which is added back also contains information about edges and other sharp transitions in the image. By infusion of this information back into the reconstruction algorithm, better quality reconstructions are achieved. Some of the published methods that utilize AL or SB do not use this "adding noise back" step [12,13,22]. Our experiments show that the addition of this step improved image quality beyond that achieved by the unconstrained SB formulation. Similar findings were reported in [15] for image denoising and deblurring applications.

In general, acceleration factors could not be increased beyond R = 4 for the resolution acquired here without causing loss of contrast and sharpness of edges, especially in the LA. As good visualization of the LA wall is essential, 3D SB TV at R = 4 is the maximum acceleration factor that could be achieved without much loss of structure and edge sharpness in the LA. At high acceleration factors of R = 4.5 and above, the reconstructed images have less edge sharpness and relatively poor quality; an example is shown in Fig. 6.

The published CS methods do not study the effect of regularization on quantification of percentage scar from post-ablation and quantification of percentage of fibrosis from pre-ablation images. We found that when the images were segmented and the quantification procedure was performed, the percentage of scar/fibrosis from the undersampled images matched those estimated from the fully sampled images. The small difference seen in the estimates were not considered significant as they were within the reported intra-user and inter-user variability [1]. To study the inter-user variability for our data, 2 out of the 4 fully sampled post-ablation images were quantified by two independent users. There was 2.5% difference on average between the estimates of the two users. It appears as though one of the users is consistently underestimating the percentage of scar, or this variation could be due to the inter-user variability in the segmentation process.

4.1. Resolution

There is a difference in resolution between the data used here and the data used in [7]. The data acquired here had a resolution of $1.25 \times 1.25 \times 2.5\ mm^3$, while the resolution in [7] was $1.4 \times 1.4 \times 1.4\ mm^3$. Having high resolution in the x–y dimension is necessary to accurately detect and analyze the thin LA wall; especially if segmentation has to be performed to quantify the images for the percentage of RF ablation induced scar or percentage of fibrosis.

4.2. Limitations and future improvements

The comparisons made in this preliminary study were based on retrospectively undersampled data. For future study it is necessary to acquire undersampled data on the scanner directly, and to acquire a large number of such prospectively undersampled datasets — the number of datasets here was limited and designed to give an initial evaluation of the approach. This work is a preliminary study to show that is possible to achieve good quality images from data acquired with acceleration factors greater than R = 3 and also show that a 3D

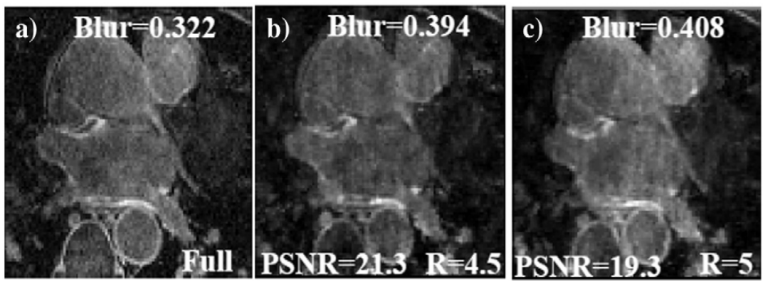

Fig. 6. An example where the acceleration factors are too high and the reconstruction algorithm fails to reconstruct images with good quality. (**a**) A slice from a fully sampled post-ablation dataset. (**b**) and (**c**) Images reconstructed using R = 4.5 and R = 5 respectively. Significant blurring is seen in the LA wall and there is also an overall loss in contrast. The MSE, blur metric and PSNR are reported on the images.

TV constraint is useful for this type of data. This work is the first to study the effect of CS based reconstruction techniques on the quantification of fibrosis/scar. Adding other constraints like the wavelet transform, low rank constraints [23] or data reordering constraints [24] could help in increasing the acceleration factors further. The downside of including additional constraints would be an increase in reconstruction time. The use of multicoil TV reconstructions, instead of the coil-by-coil reconstructions used here, could also help improve the image quality and achieve higher acceleration factors. If a multicoil TV formulation is used, the SB formulation would have to be modified as the SB framework used here cannot be directly applied to multicoil reconstructions. The existing CS techniques developed for accelerating LGE imaging of the LA [6,7] do not use a multicoil reconstruction formulation.

5. Conclusions

An SB total variation reconstruction method was developed and implemented for application to 3D LGE images of the LA. This study showed that it was possible to accelerate 3D LGE acquisitions beyond R = 3 while achieving high quality reconstructions within a short reconstruction time. The short reconstruction time of the SB approach is advantageous and might permit the method to be used in the routine clinical setting. This study showed the effectiveness of the "adding noise back" step in improving the reconstructed image quality beyond the unconstrained SB formulation.

We also analyzed the effect of accelerated acquisitions on the quantification of percentage of scar/fibrosis. The results showed that the percentage of scar or percentage of fibrosis estimated from the undersampled images matched those estimated from fully sampled data and the small variation seen was within the intra-user and inter-user variability. This implies that compared to the current 3D LGE method with GRAPPA and R = 1.7 [2,21], the data can be acquired in half of the time, which could significantly increase the usage of such LA imaging. Alternatively, higher resolution could be obtained with the current acquisition time. While further testing is needed, 3D TV with SB is a promising approach to rapidly reconstruct good quality images from undersampled (R ~ 3.5) 3D LGE LA scans.

Acknowledgments

NIH R21 HL110059. We appreciate Josh Bertola's assistance with data acquisition. We thank the anonymous reviewers whose suggestions helped greatly to improve the manuscript.

Appendix

To minimize (5)

$$\min_{m,dx,dy,dz,bx,by,bz} \left\| \sqrt{(dx)^2+(dy)^2+(dz)^2} \right\|_1 + \frac{\mu}{2}\left\| Em-k^j \right\|_2^2 + \frac{\lambda}{2}\left\| dx-\nabla_x m-bx \right\|_2^2 + \frac{\lambda}{2}\left\| dy-\nabla_y m-by \right\|_2^2 + \frac{\lambda}{2}\left\| dz-\nabla_z m-bz \right\|_2^2$$

Initialize $m^1 = E^* k^0, dx^1 = dy^1 = dz^1 = bx^1 = by^1 = bz^1 = 0$

For j=1:N1

For i=1:N2

$$m^{i+1} = F^{-1}Q^{-1}FH^i$$

$$dx^{i+1} = \max(S^i - \frac{1}{\lambda}, 0)\frac{\nabla_x m^i + bx^i}{S^i}$$

$$dy^{i+1} = \max(S^i - \frac{1}{\lambda}, 0)\frac{\nabla_y m^i + by^i}{S^i}$$

$$dz^{i+1} = \max(S^i - \frac{1}{\lambda}, 0)\frac{\nabla_z m^i + bz^i}{S^i}$$

$$bx^{i+1} = bx^i + (\nabla_x m^{i+1} - dx^{i+1})$$

$$by^{i+1} = by^i + (\nabla_y m^{i+1} - dy^{i+1})$$

$$bz^{i+1} = bz^i + (\nabla_z m^{i+1} - dz^{i+1})$$

End

$$k^{j+1} = k^j + k^0 - Em^{j+1}$$

End

Here F is the Fourier transform and $S^i = \sqrt{\left|\nabla_x m^i + bx^i\right|^2 + \left|\nabla_y m^i + by^i\right|^2 + \left|\nabla_z m^i + bz^i\right|^2}$

$$H^i = \mu E^* k^j + \lambda\nabla_x^T(dx^i - bx^i) + \lambda\nabla_y^T(dy^i - by^i) + \lambda\nabla_z^T(dz^i - bz^i)$$

and $Q = R^T R - \lambda F \Delta F^{-1}$

where m is the image being estimated, N1 is the number of outer iterations, N2 is the number of inner iterations, k the measured k-space, Δ is the Laplacian, R is the sampling pattern, d_x, d_y and d_z are dummy variables added to enforce $dx = \nabla_x m$, $dy = \nabla_y m$ and $dz = \nabla_z m$ respectively. μ is the weight on the fidelity term and λ is the weight used to enforce $d = \nabla m$ for the three directions x, y and z using SB.

Algorithm 1. The algorithm above shows the steps to reconstruct the 3D LGE images using a 3D TV constraint with Split Bregman. Derivation of these steps and implementation details are given in [10].

Appendix A. Supplementary data

Supplementary data to this article can be found online at http://dx.doi.org/10.1016/j.mri.2016.03.002.

References

[1] Oakes RS, Badger TJ, Kholmovski EG, Akoum N, Burgon NS, Fish EN, et al. Detection and quantification of left atrial structural remodeling with delayed-

enhancement magnetic resonance imaging in patients with atrial fibrillation. Circulation 2009;119:1758–67.
[2] McGann CJ, Kholmovski EG, Oakes RS, Blauer JJ, Daccarett M, Segerson N, et al. New magnetic resonance imaging-based method for defining the extent of left atrial wall injury after the ablation of atrial fibrillation. J Am Coll Cardiol 2008;52:1263–71.
[3] Peters DC, Wylie JV, Hauser TH, Kissinger KV, Botnar RM, Essebag V, et al. Detection of pulmonary vein and left atrial scar after catheter ablation with three-dimensional navigator-gated delayed enhancement MR imaging: initial experience. Radiology 2007;243:690–5.
[4] Donoho DL. Compressed sensing. IEEE Trans Inf Theory 2006;52:1289–306.
[5] Lustig M, Donoho D, Pauly JM, Sparse MRI. The application of compressed sensing for rapid MR imaging. Magn Reson Med 2007;58:1182–95.
[6] Adluru G, Chen L, Kim SE, Burgon N, Kholmovski EG, Marrouche NF, et al. Three-dimensional late gadolinium enhancement imaging of the left atrium with a hybrid radial acquisition and compressed sensing. J Magn Reson Imaging 2011; 34:1465–71.
[7] Akcakaya M, Rayatzadeh H, Basha TA, Hong SN, Chan RH, Kissinger KV, et al. Accelerated late gadolinium enhancement cardiac MR imaging with isotropic spatial resolution using compressed sensing: initial experience. Radiology 2012; 264:691–9.
[8] Akcakaya M, Basha TA, Goddu B, Goepfert LA, Kissinger KV, Tarokh V, et al. Low-dimensional-structure self-learning and thresholding: regularization beyond compressed sensing for MRI reconstruction. Magn Reson Med 2011;66:756–67.
[9] Chan TF, Golub GH, Mulet P. A nonlinear primal-dual method for Total variation-based image restoration. SIAM J Sci Comput 1999;20:1964–77.
[10] Goldstein T, Osher S. The split Bregman method for L1-regularized problems. SIAM J Img Sci 2009;2:323–43.
[11] Wu C, Tai X. Augmented lagrangian method, dual methods, and split bregman iteration for ROF, vectorial TV, and high order models. SIAM J Imag Sci 2010;3: 300–39.
[12] Bilen C, Yao W, Selesnick IW. High-speed compressed sensing reconstruction in dynamic parallel MRI using augmented Lagrangian and parallel processing. IEEE J Emerging Sel Top Circuits Syst 2012;2:370–9.
[13] Ramani S, Fessler JA, Parallel MR. Image reconstruction using augmented Lagrangian methods. IEEE Trans Med Imaging 2011;30:694–706.
[14] Yin W, Osher S, Goldfarb D, Darbon J. Bregman iterative algorithms for L1-minimization with applications to compressed sensing. SIAM J Img Sci 2008;1: 143–68.
[15] Osher S, Burger M, Goldfarb D, Xu J, Yin W. An iterative regularization method for total variation-based image restoration. Multiscale Model Simul 2005;4:460–89.
[16] Adluru G, DiBella E. Compression^2: compressed sensing with compressed coil arrays. J Cardiovasc Magn Reson 2012;14:1–2.
[17] Zhang T, Pauly JM, Vasanawala SS, Lustig M. Coil compression for accelerated imaging with Cartesian sampling. Magn Reson Med 2013;69:571–82.
[18] Crete TD F, Ladret P, Nicolas M. The blur effect: perception and estimation with a new no-reference perceptual blur metric. Proc. SPIE 6492, Human Vision and Electronic Imaging XII; 2007 [64920I].
[19] Perry D, Morris A, Burgon N, McGann C, MacLeod R, Cates J. Automatic classification of scar tissue in late gadolinium enhancement cardiac MRI for the assessment of left-atrial wall injury after radiofrequency ablation. *Proc. SPIE*, Medical Imaging 2012. Computer Aided Diagnosis; 2012 [83151D-D-9].
[20] Akkaya M, Higuchi K, Koopmann M, Burgon N, Erdogan E, Damal K, et al. Relationship between left atrial tissue structural remodelling detected using late gadolinium enhancement MRI and left ventricular hypertrophy in patients with atrial fibrillation. Europace 2013.
[21] Akoum N, Daccarett M, McGann C, Segerson N, Vergara G, Kuppahally S, et al. Atrial fibrosis helps select the appropriate patient and strategy in catheter ablation of atrial fibrillation: a DE-MRI guided approach. J Cardiovasc Electrophysiol 2011;22:16–22.
[22] Xu Y, Huang T-Z, Liu J, Lv X-G. Split Bregman iteration algorithm for image deblurring using fourth-order total bounded variation regularization model. J Appl Math 2013;2013:11.
[23] Lingala SG, Y Hu, DiBella E, Jacob M. Accelerated dynamic MRI exploiting sparsity and low-rank structure: k-t SLR. IEEE Trans Med Imaging 2011;30:1042–54.
[24] Adluru G, DiBella EV. Reordering for improved constrained reconstruction from undersampled k-space data. Int J Biomed Imaging 2008;2008:341684.

CHAPTER 4

SPLIT BREGMAN MULTICOIL ACCELERATED RECONSTRUCTION TECHNIQUE: A NEW FRAMEWORK FOR RAPID RECONSTRUCTION OF CARDIAC PERFUSION MRI

This chapter is reprinted from “Split Bregman multicoil accelerated reconstruction technique: A new framework for rapid reconstruction of cardiac perfusion MRI” by S. Kamesh Iyer, T. Tasdizen, D. Likhite, E. DiBella and published in Medical Physics, 2016 43 (4): 1969–1981. Reprinted with permission.

Split Bregman multicoil accelerated reconstruction technique: A new framework for rapid reconstruction of cardiac perfusion MRI

Srikant Kamesh Iyer
Electrical and Computer Engineering, University of Utah, Salt Lake City, Utah 84112; Scientific Computing and Imaging Institute (SCI), University of Utah, Salt Lake City, Utah 84112; and UCAIR, Department of Radiology and Imaging Sciences, University of Utah, Salt Lake City, Utah 84108

Tolga Tasdizen
Electrical and Computer Engineering, University of Utah, Salt Lake City, Utah 84112 and Scientific Computing and Imaging Institute (SCI), University of Utah, Salt Lake City, Utah 84112

Devavrat Likhite
Electrical and Computer Engineering, University of Utah, Salt Lake City, Utah 84112 and UCAIR, Department of Radiology and Imaging Sciences, University of Utah, Salt Lake City, Utah 84108

Edward DiBella[a)]
UCAIR, Department of Radiology and Imaging Sciences, University of Utah, Salt Lake City, Utah 84108

(Received 20 August 2015; revised 14 February 2016; accepted for publication 26 February 2016; published 30 March 2016)

Purpose: Rapid reconstruction of undersampled multicoil MRI data with iterative constrained reconstruction method is a challenge. The authors sought to develop a new substitution based variable splitting algorithm for faster reconstruction of multicoil cardiac perfusion MRI data.
Methods: The new method, split Bregman multicoil accelerated reconstruction technique (SMART), uses a combination of split Bregman based variable splitting and iterative reweighting techniques to achieve fast convergence. Total variation constraints are used along the spatial and temporal dimensions. The method is tested on nine ECG-gated dog perfusion datasets, acquired with a 30-ray golden ratio radial sampling pattern and ten ungated human perfusion datasets, acquired with a 24-ray golden ratio radial sampling pattern. Image quality and reconstruction speed are evaluated and compared to a gradient descent (GD) implementation and to multicoil k-t SLR, a reconstruction technique that uses a combination of sparsity and low rank constraints.
Results: Comparisons based on blur metric and visual inspection showed that SMART images had lower blur and better texture as compared to the GD implementation. On average, the GD based images had an ~18% higher blur metric as compared to SMART images. Reconstruction of dynamic contrast enhanced (DCE) cardiac perfusion images using the SMART method was ~6 times faster than standard gradient descent methods. k-t SLR and SMART produced images with comparable image quality, though SMART was ~6.8 times faster than k-t SLR.
Conclusions: The SMART method is a promising approach to reconstruct good quality multicoil images from undersampled DCE cardiac perfusion data rapidly. © *2016 American Association of Physicists in Medicine.* [http://dx.doi.org/10.1118/1.4943643]

Key words: compressed sensing, DCE imaging, multicoil imaging, cardiac perfusion, fast minimization

1. INTRODUCTION

Over 17 million people in the US are affected by coronary artery disease (CAD). Dynamic contrast enhanced (DCE) cardiac perfusion imaging with MRI is a powerful diagnostic tool for detecting CAD and assessing the amount of blood flow to the myocardium. Regions that receive the gadolinium (Gd) based contrast agent that is injected into the patient appear bright in a T1 weighted sequence due to the T1 shortening effect of Gd. Less bright regions or less rapid uptake reflects ischemia, so for accurate diagnosis, high spatiotemporal resolution is desired. One of the current methods for accomplishing relatively high spatial and high temporal resolution is to undersample the k-space data and use the time saved to improve temporal resolution. This approach leads to artifacts in image space, with the type of artifact depending on the point spread function (PSF) of the sampling pattern.

Broadly speaking, two types of approaches have been developed to handle the artifacts that arise due to undersampling k-space: (a) parallel imaging (PI) techniques and (b) compressed sensing (CS) based techniques. PI based techniques use information from multichannel receivers to remove aliasing artifacts and improve image quality. The most common PI techniques are sensitivity encoding (SENSE)[1] and generalized autocalibrating partially parallel acquisitions (GRAPPA).[2] Techniques based on the principle of CS use sparsifying transforms to improve image quality. In Ref. 3,

a combination of CS and non-linear GRAPPA (Ref. 4) was used to achieve high acceleration factors. The types of auxiliary information in SENSE reconstructions and CS reconstructions are different: coil sensitivity information in the case of SENSE reconstructions and sparsity based information in the case of CS reconstructions. Thus, their combination allows for the use of higher acceleration factors than those achieved by either SENSE or CS individually. In Refs. 5 and 6, spatial TV was used as the constraint in conjunction with SENSE, whereas in k-t sparse-SENSE,[7] a Fourier transform along the temporal dimension was used as the L_1 constraint. In Ref. 8, TV constraints were used along the spatial and temporal dimensions to drive sparsity and the cost functional was minimized using a nonlinear conjugate gradient (CG) implementation. Techniques have also been developed to incorporate motion compensation along with the sparse-SENSE formulation to improve image quality further. In Ref. 9, diffeomorphic motion compensation was performed along with a spatiotemporal TV constraint and the cost functional was minimized using an alternating projection on convex sets technique. All of the above methods, though capable of reconstructing good quality images from undersampled data, suffer from slow reconstruction speeds due to the inherent ill-conditioning of the reconstruction problem.

Recently, several methods have been proposed to accelerate the convergence of CS based methods that employ L_1 norm to drive sparsity. The fast iterative shrinkage-thresholding algorithm (FISTA)[10] and variable splitting or alternating direction method of multipliers (ADMM) based methods such as split Bregman (SB)[11] and augmented Lagrangian (AL)[12] are more popular. SB and AL methods have been shown to be nearly equivalent.[12] FISTA, SB, and AL use soft-thresholding[11] to quickly minimize the L_1 norm problem. These methods are sometimes used along with proximal operators[13] to make the cost functional easier to minimize. When the multicoil SENSE method is included with the CS method, it can be more challenging to minimize the objective function quickly. Some techniques have been developed to meet these challenges by using a combination of methods; these are detailed in the Appendix after the notation and theory are introduced in Sec. 2.A.

Here we propose to develop a new fast multicoil reconstruction algorithm that makes use of TV along the spatial and temporal dimensions as sparsifying constraints. To achieve rapid reconstructions, the proposed method uses a novel combination of SB- and FISTA-based iterative reweighting. The method is thus termed the split Bregman multicoil accelerated reconstruction technique (SMART). The performance of this type of approach for first pass myocardial perfusion imaging is evaluated.

2. THEORY AND METHOD

2.A. SMART formulation

The basic constrained sparse-SENSE cost functional can be written as

$$\underset{m}{\operatorname{argmin}}\ \lambda_1\|\varphi_1 m\|_1+\lambda_2\|\varphi_2 m\|_1+\frac{\mu}{2}\sum_{i=1}^{N\text{Coils}}\|EC_i m-k_i\|_2^2, \quad (1)$$

where E is an encoding matrix that includes the sampling pattern and the Fourier transform, C is the complex coil sensitivity maps, k is the measured k-space data, μ is the weight on the multicoil fidelity constraint, $\|\|_1$ is the L_1 norm, and $\|\|_2$ is the L_2 norm. A single set of images m that satisfies the multicoil fidelity constraint and the sparsity constraint is estimated, instead of estimating a different image for each coil. φ_1 and φ_2 are constraints that help in driving sparsity of the reconstructed images in some transformation domain.

To utilize the spatial and temporal correlations in the data, we use TV for constraints along the spatial and temporal dimensions.

Hence Eq. (1) can be rewritten as

$$\underset{m}{\operatorname{argmin}}\ \lambda_1\left\|\nabla_{xy} m\right\|_1+\lambda_2\|\nabla_t m\|_1+\frac{\mu}{2}\sum_{i=1}^{N\text{Coils}}\|EC_i m-k_i\|_2^2, \quad (2)$$

where ∇_{xy} is the spatial gradient operator and ∇_t is the temporal gradient operator. μ, λ_1, and λ_2 are weights that control the amount of fidelity constraint, spatial regularization, and temporal regularization, respectively. Applying the SB-based variable splitting technique to Eq. (2) by using surrogate variables S, T, and P, such that $S=\nabla_{xy} m$, $T=\nabla_t m$, and $P_i=C_i m$, allows Eq. (2) to be rewritten as

$$\begin{aligned}\underset{m,S,T,P,\hat{S},\hat{T},\hat{P}}{\operatorname{argmin}}\ &\lambda_1\|S\|_1+\lambda_2\|T\|_1+\frac{\mu}{2}\sum_{i=1}^{N\text{Coils}}\|EP_i-k_i\|_2^2\\&+\frac{\alpha_1}{2}\left\|S-\nabla_{xy} m-\hat{S}\right\|_2^2+\frac{\alpha_2}{2}\left\|T-\nabla_t m-\hat{T}\right\|_2^2\\&+\frac{\beta}{2}\sum_{i=1}^{N\text{Coils}}\left\|P_i-C_i m-\hat{P}_i\right\|_2^2. \quad (3)\end{aligned}$$

$\hat{S}$, $\hat{T}$, and $\hat{P}$ come from optimizing the Bregman distance.[11] The image m that is being estimated has been decoupled from the L_1 norm terms and is present only in L_2 norm based terms. Hence, when trying to minimize Eq. (3) with respect to m, only the L_2 norm terms remain,

$$\begin{aligned}\underset{m}{\operatorname{argmin}}\ &\frac{\alpha_1}{2}\left\|S-\nabla_{xy} m-\hat{S}\right\|_2^2+\frac{\alpha_2}{2}\left\|T-\nabla_t m-\hat{T}\right\|_2^2\\&+\frac{\beta}{2}\sum_{i=1}^{N\text{Coils}}\left\|P_i-C_i m-\hat{P}_i\right\|_2^2. \quad (4)\end{aligned}$$

Similarly, the surrogate variable P is present only in L_2 norm terms,

$$\underset{P}{\operatorname{argmin}}\ \sum_{i=1}^{N\text{Coils}}\|EP_i-k_i\|_2^2+\frac{\beta}{2}\sum_{i=1}^{N\text{Coils}}\left\|P_i-C_i m-\hat{P}_i\right\|_2^2. \quad (5)$$

Equations (4) and (5) can be quickly minimized using the acceleration scheme in FISTA.

The FISTA algorithm defines a sequence of weights,

$$t_0=1, t_{n+1}=\frac{1+\sqrt{1+4t_n^2}}{2};\quad n=0,1,2,\ldots. \quad (6)$$

Given any two successive sets of estimates Z^{n+1} and Z^n, FISTA helps to improve the estimate by the following step:

$Z^{n+1}_{\text{IMPROVED}} = Z^{n+1} + ((t_n - 1)/t_{n+1})(Z^{n+1} - Z^n)$ to accelerate convergence. The new improved estimate is fed back into the iterative reconstruction algorithm.

The L_1 norm terms are given by

$$\underset{S}{\text{argmin}}\, \lambda_1 \|S\|_1 + \frac{\alpha_1}{2}\|S - \nabla_{xy} m - \hat{S}\|_2^2, \tag{7}$$

$$\underset{T}{\text{argmin}}\, \lambda_2 \|T\|_1 + \frac{\alpha_2}{2}\|T - \nabla_t m - \hat{T}\|_2^2. \tag{8}$$

The L_1 norm terms that contain S and T can be minimized using soft-thresholding.[11]

$\hat{S}$, $\hat{T}$, and $\hat{P}$ are minimized using a linear update step.

$$\hat{P}^{k+1} = \hat{P}^k + (C_i m - P_i), \tag{9}$$

$$\hat{S}^{k+1} = \hat{S}^k + (\nabla_s m - S), \tag{10}$$

$$\hat{T}^{k+1} = \hat{T}^k + (\nabla_t m - T). \tag{11}$$

SMART has been specifically designed to handle reconstruction problems where spatial and temporal constraints have to be used simultaneously. This method uses one fewer substitution compared to Ref. 14 and does not use any of the matrix factorization or inversion techniques used in Refs. 14 and 15. The method developed here is tested on prospectively undersampled radial DCE cardiac perfusion images as opposed to the SB/AL methods developed in Refs. 14 and 15 which were tested on retrospectively undersampled Cartesian data. A regridding technique is used here to interpolate the radial k-space data to a Cartesian grid prior to reconstruction for faster iterations, though the proposed method is compatible with methods using the nonuniform fast Fourier transform (NUFFT) to regrid at every iteration.[16]

DCE cardiac perfusion images have high correlations along the temporal dimension such that a gradient operator along the temporal direction can be used as a good sparsifying transform. When combined with spatial TV, this has been shown to be effective at reconstructing radial DCE cardiac perfusion data.[17] The resolution and correlations along the spatial and temporal dimensions for DCE cardiac perfusion images are generally not the same. Hence it is important to keep the spatial and temporal constraints separate, with separate weightings, instead of using a combined spatiotemporal 3D filtering kernel,[18] in order to control how much regularization is performed along each dimension.

2.B. Data acquisition

2.B.1. ECG-gated dog datasets

Cardiac perfusion data have been acquired at rest on a 3T Verio scanner using a saturation recovery turboFLASH sequence with TR/TE = 2.5/1.4 ms, FOV = 260 mm^2, 1.8 × 1.8 × 8 mm resolution. One saturation pulse per set of four slices is used, so the saturation recovery time for the readout of the first ray is ~21 ms. A 30-ray golden ratio radial sampling pattern is used, and 100–120 time frames are acquired using a 32-channel phased array coil. The animal study has been performed for a separate study investigating atrial fibrillation, which did not require perfusion data. The contrast agent gadolinium-BOPTA, 0.05 mmol/kg, is used and the proposed reconstruction method is tested on nine dog datasets. Institutional Animal Care and Use Committee (IACUC) approval has been obtained.

2.B.2. Ungated human data

The SMART method is tested on ten ungated human datasets (seven rest perfusion and three stress perfusion datasets) acquired with Institutional Review Board (IRB) approval. The data have been acquired on a Siemens 3 T Verio scanner using a saturation recovery radial turbo-FLASH sequence with TR/TE = 2.2/1.2 ms, FOV = 280 mm^2. One saturation pulse is used per set of 4–5 slices so that the saturation recovery time for the readout of the first ray is ~26 ms. A 24-ray golden ratio, radial sampling pattern is used to acquire the data, and the acquisition matrix is of size 288 × 24. Four to five slices and 220–250 time frames are acquired using a 32-channel phased array coil with a voxel size of 2.3 × 2.3 × 8 mm resolution. The contrast agent gadoteridol, 0.06 mmol/kg, is used for both rest and stress perfusion.

2.C. Coil compression and k-space data interpolation

Data compression using principal component analysis (PCA)[19,20] is first performed on the measured k-space data to compress the data to eight virtual coils. Coil compression reduces the reconstruction time. A regridding technique is applied to interpolate the radial k-space data onto a Cartesian grid,[21] and the k-space data in Eq. (1) replaced with these interpolated data. This regridding technique allows for faster iterations compared to an implementation that regrids at every iteration to match the measured k-space data. The reconstruction and analysis discussed below are performed on interpolated k-space data.

2.D. Generation of coil sensitivity maps

2.D.1. ECG-gated datasets

To generate coil sensitivity maps for the ECD-gated dog datasets, reference images for each coil are generated by combining 250 unique rays from the postcontrast frames starting from the final postcontrast time frame. As a golden ratio acquisition is used, these rays are nonoverlapping. The number of rays is chosen to be large enough to give good reference images. The coil sensitivity maps are robust to changes in the number of rays chosen for the reference image. The number of rays can be varied from 200 to 300. An IFT of the interpolated k-space data is used to generate the reference images. These reference images are then used to compute the coil sensitivity maps using an eigenvector method described in Ref. 22.

2.D.2. Ungated human datasets

Unlike the ECG-gated dog datasets where each slice has a consistent cardiac phase, the ungated human datasets have data from different cardiac phases in the same slice acquisition.

Additional steps are required to reconstruct the ungated human datasets. Binning the data into near-systolic and near-diastolic frames mitigates motion in the data to some extent, which helps to enforce temporal sparsity as the temporal correlations for the binned data are higher than for the unbinned dataset. This binning process helps in the estimation of coil sensitivity maps and improved image quality.

2.D.2.a. Steps to bin the ungated data into near-systolic and near-diastolic frames. To segregate the ungated data into near-systolic and near-diastolic frames, an initial reconstruction is first performed using a gradient descent (GD) based implementation of Eq. (2) by treating the entire ungated dataset as k_i. A temporary coil sensitivity map is generated by combining several postcontrast time frames, and using the IFT as a reference image. The same coil sensitivity map is used for both near-systolic and near-diastolic frames as no binning information is available at this stage. The data are then binned into near-systolic and near-diastolic frames using the self-gating method described in Ref. 23 using the initial set of reconstructions. The steps for this binning operation are shown in Fig. 1. A small rectangular region is cropped around the heart, and the sum over the region is calculated. The peaks and troughs of the 1D signal thus computed are used to bin data points into near-diastolic and near-systolic time frames, respectively.

Alternative binning methods could have been used instead of an initial reconstruction based on a gradient descent implementation for binning as described above. Faster binning of the ungated dataset could have been performed by generating images using the IFT of the interpolated k-space data and combining the images using a square-root-sum-of-squares (SSOS). In order to test whether the binning process helped in improving image quality as compared to performing reconstructions from the unbinned dataset, reconstructions had to be performed on the unbinned dataset based on Eq. (2) from the unbinned data. As the GD images thus generated were available, they were used to bin the data. The binning methods are further discussed in Sec. 4.A.

2.D.2.b. Computing coil sensitivity maps after binning is performed. After the binning process is performed, reference images for each coil are generated by combining k-space data from multiple postcontrast frames such that the reference

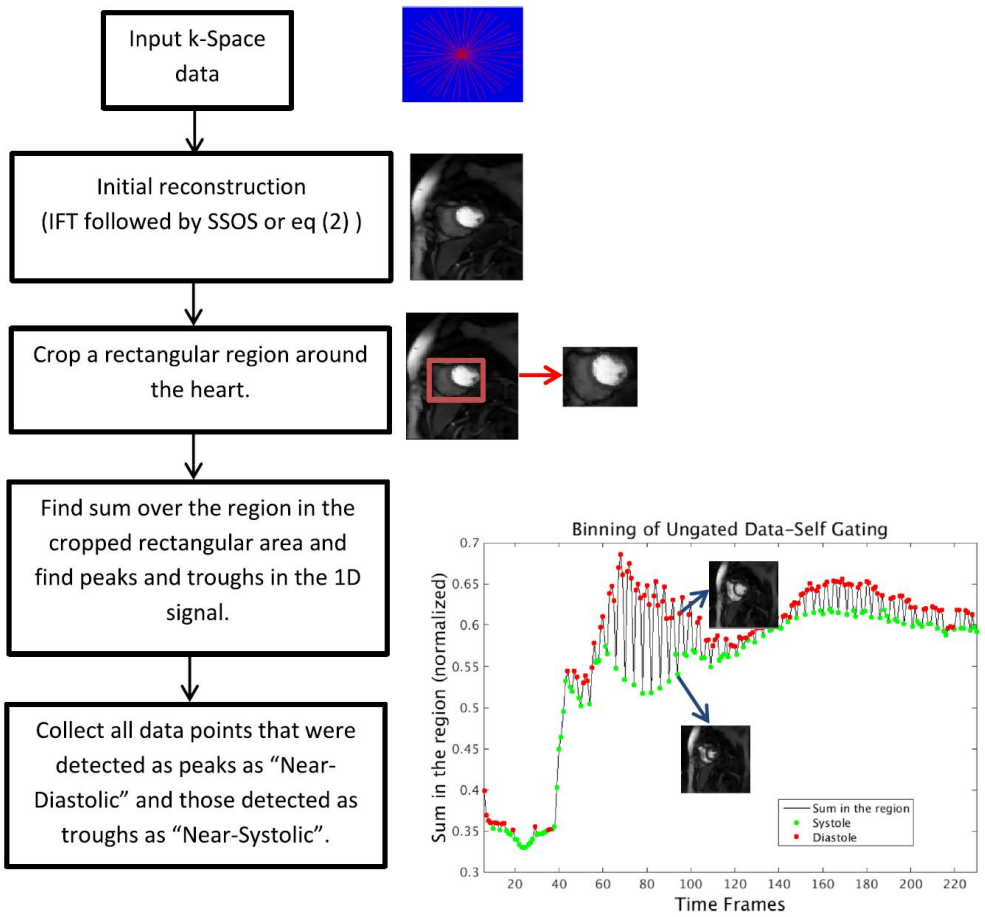

FIG. 1. Flow chart showing the steps followed to bin the data into near-diastolic and near-systolic frames to reduce the effects of motion on image reconstructions.

frame has 250 unique rays. This process is performed for the near-systolic and near-diastolic frames separately. The eigenvector method described in Ref. 22 is then used to generate the coil sensitivity maps from the multiple reference images. Hence the near-diastolic and near-systolic datasets have their own coil sensitivity maps.

2.E. Implementation of reconstruction

The method has been implemented in MATLAB and runs on a computer with an Intel Xeon E5620 CPU with a processor base frequency of 2.4 GHZ, 32 cores, a total dedicated memory of 96 GB.

2.E.1. Choosing regularization parameters for SMART

2.E.1.a. Radial datasets. For the ECG-gated dog datasets, the weights are chosen as $\lambda_1 = 0.000\,75$, $\lambda_2 = 0.09$, $\mu = 0.3$, $\alpha_1 = 0.035$, $\alpha_2 = 0.035$, and $\beta = 0.09$. For the ungated human datasets, the weights for the reconstruction are chosen as $\lambda_1 = 0.01$, $\lambda_2 = 0.35$, $\mu = 0.2$, $\alpha_1 = 0.01$, $\alpha_2 = 0.01$, and $\beta = 0.7$. The weights are chosen based on a test dataset. The weights chosen allow for rapid convergence and give good image quality. The number of iterations is set to 50. The weights chosen for the ECG-gated dog data and the ungated human data are different because these are quite different types of data. In particular, the amount of motion, and also SNR, number of rays, and resolution are different between the two types of acquisitions. Hence the weights are different for each of the data types.

2.E.1.b. Retrospectively undersampled Cartesian dataset. For the retrospectively undersampled Cartesian data, the weights μ and λ_1 are empirically set as $\mu = 0.5$ and $\lambda_1 = 0.025$. The reconstructions are repeated for various values of λ_2 and the optimal weight λ_2 is finally set as the value that minimizes the normalized mean squared error (NMSE) between the fully sampled image and reconstructed image. The optimal weight for λ_2 is found to be $\lambda_2 = 0.01$.

2.E.2. Comparison of reconstruction methods

The proposed reconstruction method is compared with a gradient descent based implementation of Eq. (2) and the multicoil k-t SLR method[24] (available at https://research.engineering.uiowa.edu/cbig/content/matlab-codes-k-t-slr). The multicoil k-t SLR method uses a combination of low rank constraints and spatiotemporal TV constraints to drive sparsity. An augmented Lagrangian[14] variable substitution method is used to accelerate the convergence of the multicoil k-t SLR reconstructions. SMART and multicoil k-t SLR reconstruction methods are also tested on a fully sampled Cartesian dataset that is undersampled with a 16-ray golden ratio sampling pattern. The normalized mean squared errors are calculated for each method.

2.E.3. Choosing regularization parameters for k-t SLR

There are four weights that are set for k-t SLR. The input data are normalized so that the maximum magnitude of the k-space data is fixed to 2.5×10^{-5}. The values of p and α are set to $p = 0.1$ and $\alpha = 4$, as in Ref. 24. The other two weights are chosen as follows.

2.E.3.a. Radial datasets. For the ECG-gated dog datasets, the weights are chosen as $\lambda_1 = 10^{-9}$ and $\lambda_2 = 2\times10^{-8}$. For the ungated human datasets, the weights for the reconstruction are chosen as $\lambda_1 = 2\times10^{-9}$ and $\lambda_2 = 0.75\times10^{-8}$. The weights are empirically chosen to achieve the best visual image quality.

2.E.3.b. Retrospectively undersampled Cartesian dataset. For the retrospectively undersampled Cartesian data, the weight λ_2 is set to $\lambda_2 = 4\times10^{-8}$. For the final free weight, λ_1, the reconstructions are repeated for various values of λ_1 and the optimal weight λ_1 is set as the value that minimizes the normalized mean squared error between the fully sampled image and reconstructed image. The optimal weight for λ_1 is found to be $\lambda_1 = 5\times10^{-9}$.

The three reconstruction methods are compared in terms of reconstruction speed and image quality based on visual inspection and the use of a blur metric.[25] The blur metric is a reference image-free metric that quantifies the amount of blur in the image. The intensity variations (the absolute value of the gradient) between neighboring pixels of a low-pass filtered version of the image are compared with the intensity variations between neighboring pixels of the original image. The greater the difference between the two, the sharper the image. The blur metric is normalized to a range of 0–1, with larger values meaning more blurring in the image. A detailed explanation of the blur metric is in Ref. 25.

3. RESULTS

3.A. Comparison with GD based implementations

3.A.1. Reconstruction of ECG-gated dog datasets

The images reconstructed using the SMART implementation have slightly better texture and image quality compared to the gradient decent based implementation of Eq. (2), which is reflected in lower blur metric values for the SMART reconstructions compared to the GD implementation. The values are reported along with the images. Comparisons are also made with images reconstructed on each coil data independently and combined using SSOS to better assess the effect of infusing coil sensitivity information into the reconstruction algorithm. A comparison of the images in Fig. 2 shows that the multicoil images are better at reconstructing fine structures compared to SSOS reconstructions. The white arrow shows the region where multicoil reconstructions are sharper and the structures are better visualized. Between the two multicoil reconstruction methods, the SMART reconstructions tend to have better texture, and the smoothing of uniform regions that is seen in the gradient descent based reconstructions is generally avoided.

3.A.2. Reconstruction of ungated human datasets

3.A.2.a. Performing reconstructions on unbinned data. The measured k-space data that are acquired from the scanner using the free-breathing ungated[26] acquisition method have

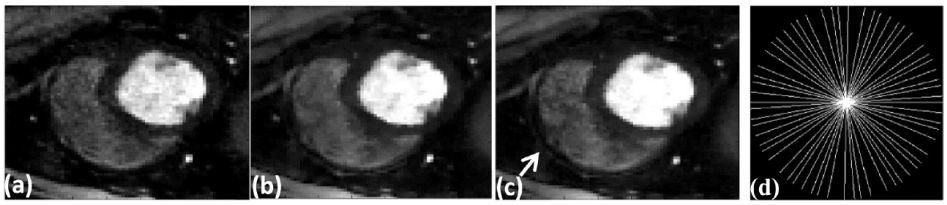

FIG. 2. Images comparing the effect of including coil sensitivity information in the reconstruction. Reconstructions were performed on a 30-ray per time frame dog dataset. (a) Each coil reconstructed individually and combined using SSOS, (b) multicoil reconstruction using gradient descent, (c) multicoil reconstruction using the proposed SMART method, and (d) one frame of the 30-ray sampling pattern used to acquire the data. The white arrow shows the region where the SSOS image is missing a structure and the multicoil images have performed better at reconstructing the structure more faithfully.

time frames of the same slice acquired during different cardiac phases. When reconstructions are performed on the unbinned data, interframe motion in the underlying data causes motion blur in parts of the reconstructed images. Also, in some cases, the excess motion causes a faint false edge to be added to the images due to the use of temporal gradients as constraints. Our experiments show that it is better to perform binning or self-gating to segregate data into near-systolic and near-diastolic frames before reconstruction is performed. An example is shown in Fig. 3. The arrow shows the region where a structure has been smoothed in the unbinned reconstructions whereas the structure has been preserved in the binned reconstructions.

3.A.2.b. Performing reconstruction on binned data. A comparison of the reconstructed images shows that the SMART reconstructions have better texture in uniform regions such as the liver and in the right ventricle (RV) blood pool compared to GD based reconstructions, though overall image quality is similar. An example is shown in Fig. 4. The SMART based images have less blur compared to GD reconstructions, shown by the lower blur metric values reported along with the images. Further comparison using the blur metric is shown in Fig. 5. Figure 5(a) shows a comparison of the blur metric computed from one slice. The black curve, which corresponds to blur metric computed from GD images, is higher for all the time points when compared with the red curve, which corresponds to the blur metric computed using SMART. The blur metric for all ten datasets is shown in Fig. 5(b). GD and SMART have significantly different blur metric, $p < 0.05$.

3.A.3. Reconstruction time

The images reconstructed using the SMART based reconstruction method need ~35 iterations to meet the convergence criterion $\left(\left\|m^k - m^{k-1}\right\| / \left\|m^{k-1}\right\|\right) * 100 \leq 0.01$. An example is shown in Fig. 6. At the 35th iteration, the curve drops to below 0.01. To be conservative, we set the number of iterations to 50 for all datasets. For a dataset of size (288,288,100), the reconstruction time using the SMART method is ~(424 ± 18) s, whereas that of a GD based implementation is ~(2614 ± 77) s. This corresponds to a speedup up of ~6 compared to the GD based method.

3.B. Comparisons with multicoil k-t SLR

3.B.1. Reconstruction on Cartesian data retrospectively undersampled with a 16-ray golden ratio sampling pattern

A comparison of images in Fig. 7 shows that both the SMART and multicoil k-t SLR methods perform well at reconstructing the image. Both of these methods are able to reconstruct the different structures faithfully, when compared to the fully sampled image in Fig. 7(a). The magnitude of the image difference shown in Figs. 7(d) and 7(e) appears mostly as noise. The overall image quality of both these methods is similar, as reflected in the NMSE reported in Fig. 7.

3.B.2. Reconstruction of gated dog data

The images in Fig. 8 show two time frames from a gated dog dataset that are reconstructed using multicoil k-t SLR [Figs. 8(a) and 8(c)] and SMART [Figs. 8(b) and 8(d)], respectively. The blur metric values are reported along with the images. There is a very little difference in the blur metric estimated on the images reconstructed by the two

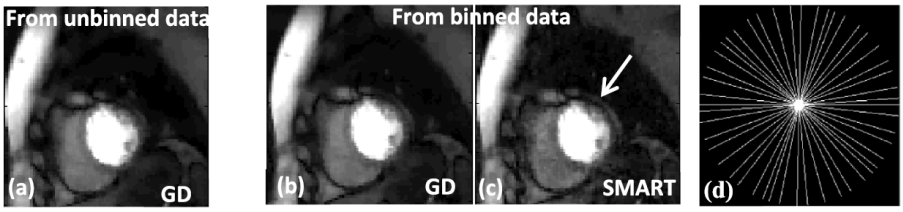

FIG. 3. The effect of binning to near-diastole and near-systole prior to reconstruction on image quality. (a) Image from unbinned data, reconstructed using GD implementation. (b) and (c) images from binned data using GD and SMART, respectively. The arrow shows the region where there is blurring in the image reconstructed using the unbinned data. Between the SMART image and GD image for binned data, the SMART image has better texture, and smoothing of uniform regions in the image has been avoided. (d) One frame of the 24ray sampling pattern used to acquire the data.

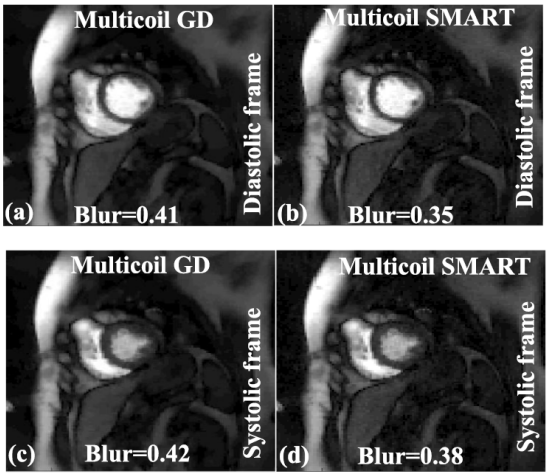

FIG. 4. A comparison of multicoil images reconstructed using GD and SMART methods. A systolic and a diastolic frame are shown for the two reconstructions. The blur metric values are reported along with the images. The SMART reconstructions in (b) and (d) have better texture compared to the GD reconstructions in (a) and (c), which is reflected in the lower blur metric values for SMART images.

methods. Both the SMART and k-t SLR techniques are able to reconstruct high quality images, and the sharpness of the edges in the myocardium is well maintained. For a dataset of size (288,288,100), the reconstruction time using the multicoil k-t SLR method is ~2879 s, which is ~6.8 times slower than the SMART technique.

4. DISCUSSION

A new multicoil reconstruction method that utilizes SB and FISTA to achieve fast convergence is presented. The SMART method is developed for imaging schemes that need to use both spatial and temporal constraints simultaneously. Though the method is developed for the use of total variation along the spatial and temporal domains as the constraints, it is general enough to be used with many sparsifying transforms. The proposed method does not involve any complex matrix inversion or factorization techniques. A SB based variable substitution is used to allow for fast minimization of the optimization problem. Since the SMART method uses one fewer-variable substitution as compared to Ref. 14, the memory footprint of the proposed method is slightly lower. The SMART method has been tested on prospectively undersampled 30-ray radial ECG-gated dog cardiac perfusion data and 24-ray radial ungated human cardiac perfusion data, whereas the existing SB/AL based methods[14,15] have been tested only on retrospectively undersampled data.

The SMART formulation has been compared to a steepest descent (GD) based implementation and multicoil k-t SLR in terms of speed and image quality. Overall, the quality of images from the SMART based method and the GD based implementation is similar, though the images reconstructed using the SMART based method have lower blur and better texture in uniform regions, which is seen from the lower blur metric values found with the SMART based method (Fig. 5). Variation in the blur values is mostly due to the use of soft-thresholding in the SB based implementation of SMART as opposed to the use of an approximation to the L_1 norm in the GD based implementation. The smooth approximation of the TV term used for GD based implementations is given by $|\nabla m|_1 \approx \sqrt{|\nabla m|^2 + \beta^2}$, where β^2 is a positive constant. By adding a positive constant, the smooth approximation of the L_1 norm helps in preventing singularities but becomes a poor approximation of the L_1 norm as the positive constant becomes larger.[27]

The multicoil k-t SLR reconstruction uses an AL based implementation and did not use the smooth approximation of TV. Hence the loss of texture and increase in blur that is seen in GD implementation are not seen in k-t SLR based reconstructions. Both SMART and k-t SLR are able to reconstruct images with good image quality. The k-t SLR method uses a low rank constraint along with a spatiotemporal TV constraint to improve image quality. The SMART technique uses only TV along the spatial and temporal dimensions and does not use any low rank constraints. Though SMART and k-t SLR both use fast minimization techniques, there is a large difference in the reconstruction time. This is mainly due to the use of low rank constraint in the k-t SLR. In time frames where there is contrast in the blood pool-myocardium region, the image quality of k-t SLR and SMART techniques is similar. In some postcontrast time frames, we found small improvements in the texture of uniform regions in areas such as lungs. This resulted in a small change in the blur metric estimated from the k-t SLR reconstructions and SMART reconstructions, as reported in Figs. 8(c) and 8(d).

There is a difference in the way spatiotemporal TV is performed by SMART and k-t SLR. The TV constraint in SMART is implemented as $\lambda_1\|\nabla_s m\|_1 + \lambda_2\|\nabla_t m\|_1$, while the k-t SLR implementation uses $\lambda\sqrt{|\nabla_s|^2 + \alpha|\nabla_t|^2}$. In both these techniques, the amount of spatial and temporal regularizations that is applied can be individually controlled. But these are two different ways of implementing spatiotemporal TV and the overall performance may differ depending on the type of data.

One major problem that multicoil reconstructions face is slow reconstruction speed. The L_1 norm based multicoil reconstruction is inherently ill-posed and in general is slow to converge. The proposed method uses variable substitution based on a SB framework to separate the coil sensitivity maps from the fidelity constraint. Similarly, SMART uses the principle of variable substitution in the L_1 norm terms to decouple the image being estimated from the coil sensitivity map and also the L_1 norm term. The use of soft-thresholding then allows for fast minimization of the L_1 norm subproblems. The FISTA based iterative reweighting scheme allows rapid minimization of the rest of the L_2 norm based terms. Compared to the GD based implementation, the SMART based formulation has a speedup of ~6.

Acquiring good quality DCE cardiac perfusion images can sometimes be challenging, especially when the cardiac gating

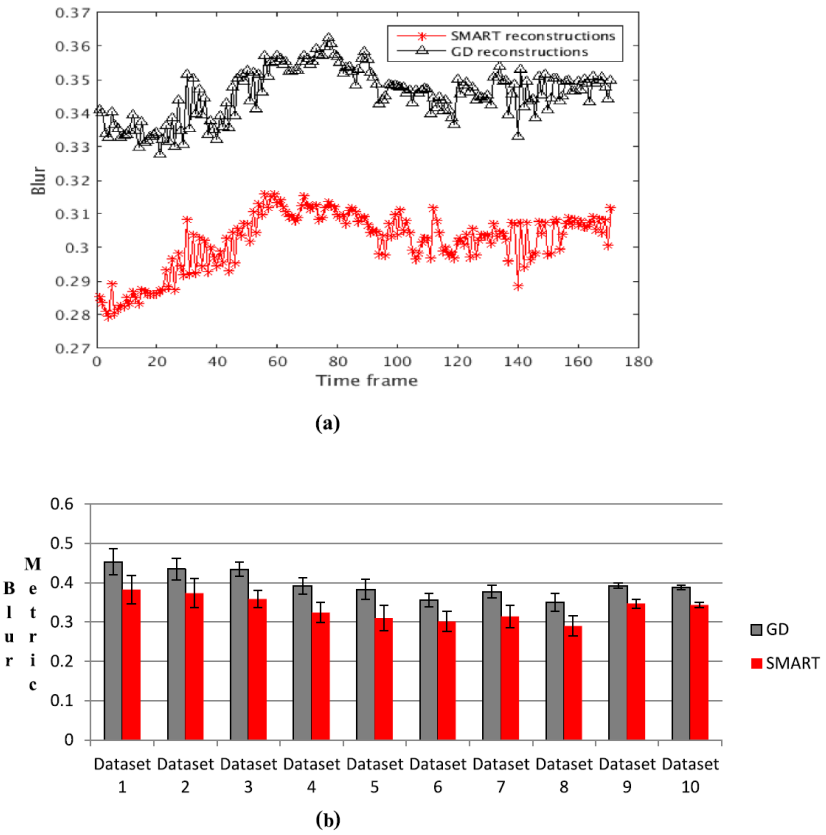

FIG. 5. Blur metric values for the images reconstructed using SMART and GD based methods. A value close to 1 for the blur metric means that the image is highly blurred whereas a value close to 0 means that the image is very sharp. (a) Blur metric comparison between SB and GD computed on a single slice. (b) A comparison of the average blur metric for the ten datasets, and the mean and standard deviation are reported. In both cases, the blur metric calculated from the GD images is higher than the SMART based reconstructions (see color online version).

signal is difficult to accurately detect.[23,26] Challenges with good gating signals at 3 T has led to the development of ungated[23,26] acquisition methods that do not use the cardiac gating signal but instead use self-gating[23] to bin the data into

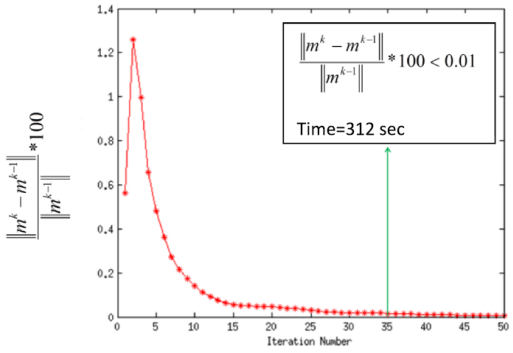

FIG. 6. Rapid convergence of the SMART based method is shown. At 35th iteration, the relative change in the image between two successive iterations drops below 0.01%. For a dataset of size (288,288) and 100 time frames, the time taken for completing 35 iterations is ~296 s and for 50 iterations is ~424 s.

near-systolic and near-diastolic time frames postacquisition. More details of the ungated DCE cardiac MR acquisition technique are given in Ref. 23. Though the SMART formulation has been tested on ten human ungated DCE cardiac perfusion datasets and high quality images have been reconstructed, the acquisition of ungated DCE cardiac perfusion images is relatively new and the SMART reconstruction method for ungated DCE data can likely be improved by including motion or using temporally varying weights. That is, there are temporal correlations in the underlying images that can be utilized to drive sparsity. The presence of motion in the data hinders this process. For the ungated human datasets, the best results are obtained when binning is performed prior to reconstruction to segregate the data into near-systolic and near-diastolic frames, which mitigates the effects of cardiac motion. Instead of using only two bins to segregate ungated data into near-systolic and near-diastolic frames, using multiple bins to separate data that are parts of different cardiac cycles could mitigate the problem further without the explicit use of motion compensation techniques.[9,28–30] Motion compensation techniques[9,28–30] have been shown to perform well in reconstructing good quality images, but using

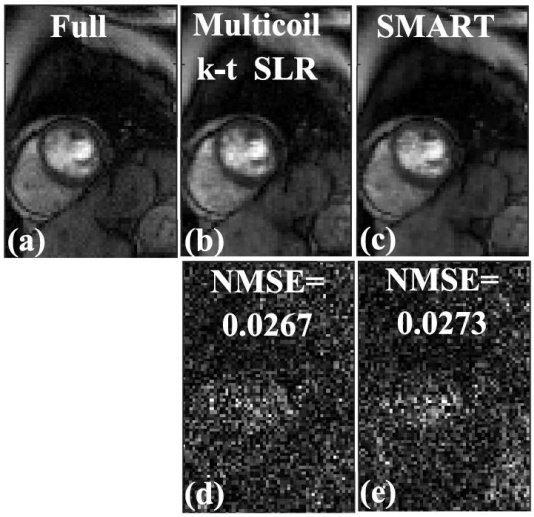

FIG. 7. Comparison of SMART and multicoil k-t SLR on a Cartesian dataset retrospectively undersampled with a 16-ray golden ratio sampling pattern. (a) Truth from the fully sampled Cartesian k-space data, (b) image reconstructed using multicoil k-t SLR, and (c) image reconstructed using SMART. (d) Magnitude of the image difference between multicoil k-t SLR in (b) and the fully sample image in (a). (e) Magnitude of the image difference between SMART in (b) and the fully sample image in (a). The normalized mean squared error (MSE) is reported along with the difference image. Both SMART and k-t SLR performed well at reconstructing the image and had similar image quality.

these methods adds an additional level of computational complexity and greatly reduces the reconstruction speed. Another improvement to the SMART technique could be the use of temporally varying weights instead of a constant weight for all time points. As the shape of the heart and the amount of motion change from frame to frame, it might be better to use temporally varying weights that are data dependent. An initial reconstruction could also be used as a reference image to estimate these weights. Similar approaches based on spatially varying weights have been used in Refs. 31 and 32 and have shown improvements in image quality.

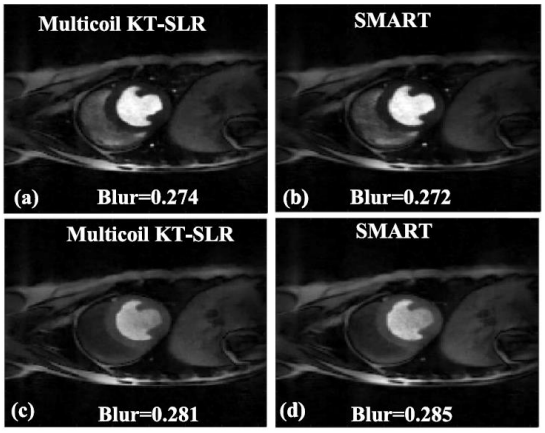

FIG. 8. Comparison of the proposed SMART with multicoil k-t SLR. The reconstructions were performed on a 30-ray dog dataset; two time frames are shown. [(a) and (c)] Images reconstructed using multicoil k-t SLR. [(b) and (d)] Images reconstructed using SMART. The blur metric values are reported along with the images. The quality of images in (a) and (c), which were reconstructed using multicoil k-t SLR, is similar to the images in (b) and (d), which were reconstructed using SMART. This is reflected in the blur metric.

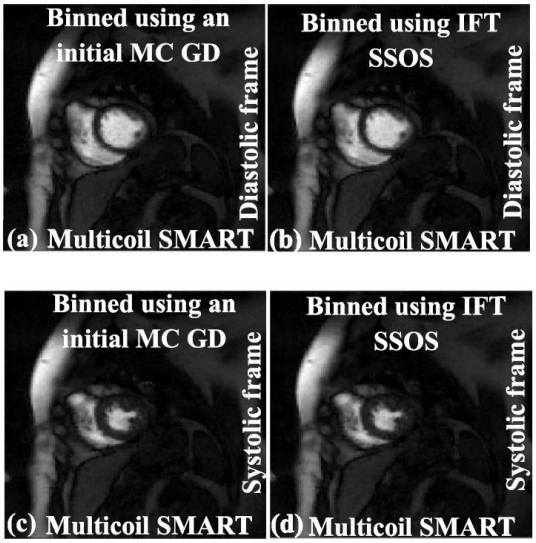

FIG. 9. Effect of binning using IFT SSOS as the initial estimate instead of using GD implementation of Eq. (2). The IFT SSOS images take less time to compute compared to multicoil GD images. (a) and (c) show SMART reconstructions with the binning process being performed using the GD implementation of Eq. (2). (b) and (d) show SMART reconstructions with the binning process being performed using IFT SSOS images. The image quality for both the binning methods is similar, which shows that using IFT SSOS as the initial estimate for binning is a viable option.

4.A. Faster prereconstruction binning strategies

To bin or self-gate the ungated data into near-systolic and near-diastolic frames for improved reconstructions, an initial set of images is generated using a GD implementation of Eq. (2). Faster methods can be used to bin the data. For example, the IFT of the k-space data followed by SSOS can be used as an initial estimate to bin the ungated dataset instead of GD images. A comparison is shown in Fig. 9; diastolic and systolic time frames are shown. The images in Figs. 9(a) and 9(c), which are generated using SMART after the binning process is performed using GD images, are similar in image quality to the images in Figs. 9(b) and 9(d), which are generated using SMART after the binning process is performed using IFT SSOS images. As the main focus of this paper is not the binning process, other binning techniques such as using the center of k-space for binning or using the sinograms are not investigated.

4.B. Improvements using "adding noise back step"

The "adding noise step" derived in Ref. 11 using the application of Bregman distance has been shown to improve image

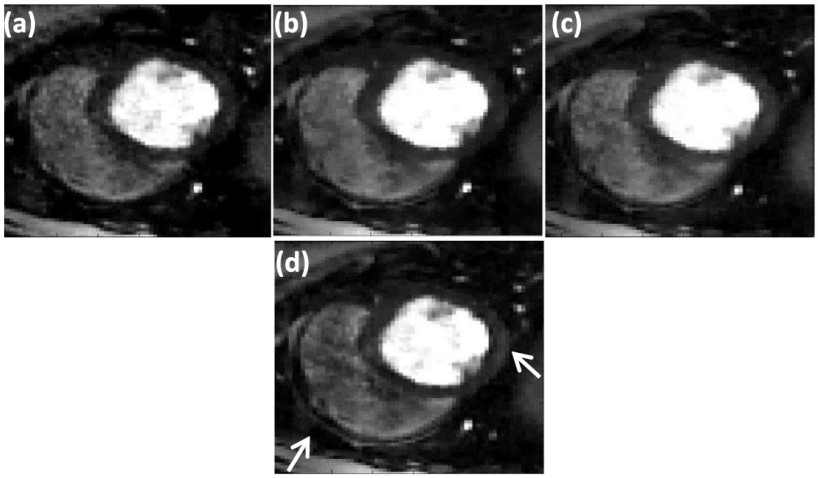

FIG. 10. Improving image quality by using "adding noise back" step (Ref. 11). The reconstructions were performed on a 30 ray dog dataset. Reconstructions using (a) SSOS, (b) GD, (c) SMART method, and (d) SMART with the additional adding noise back step. The white arrow shows the region where the adding noise back step has helped to improve image sharpness beyond that achieved by SMART alone.

sharpness for some applications such as image denoising. The multicoil version of this adding noise back step is given by

$$\min_{m,P,S,T,\hat{P},\hat{S},\hat{T}} \frac{\mu}{2}\sum_{i=1}^{N\text{Coils}} \|EP_i - k_i\|_2^2 + \lambda_1\|S\|_1 + \lambda_2\|T\|_1 + \frac{\beta}{2}\sum_{i=1}^{N\text{Coils}} \left\|P_i - C_i m - \hat{P}_i\right\|_2^2 + \frac{\alpha_1}{2}\left\|S - \nabla_s m - \hat{S}\right\|_2^2 + \frac{\alpha_2}{2}\left\|T - \nabla_t m - \widehat{T}\right\|_2^2, \quad (12)$$

$$k_i^{l+1} = k_i^l + \left(d_i^0 - EC_i m\right). \quad (13)$$

Equation (13), where the difference between the estimated image m and the measured k-space d_i^0 is added back to the measured k-space, is called the adding noise back step. This step helps to maintain fine texture and sharp features, which could be lost by using TV. We applied this step to the SMART formulation to test the effect on image quality. An example of SMART with the adding noise back step applied to a gated dataset is shown in Fig. 10. A comparison of the images shows that the use of this adding noise back step improves the sharpness of features of some regions [white arrow in Fig. 10(d)]. When the SMART formulation with the adding noise back step is applied to ungated human datasets, the change in image quality is minimal. As compared to the gated dog datasets, the ungated human datasets have lower resolution, lower SNR, and fewer rays. In addition, the ungated human datasets have a lot of motion. Since these are quite different types of data, the effect of the adding-noise-back step is different on the two types of data.

4.C. Limitations

The proposed SMART method uses variable substitution to decouple the image being estimated from the L_1 norm term. As the method uses variable substitution in the two L_1 norm terms and also in the fidelity norm term, the method tends to be memory intensive as compared to the GD based implementation. Cost and availability of computers with large memory are generally not an issue, but still should be considered before choosing a reconstruction algorithm.

5. CONCLUSION

A new fast multicoil reconstruction method is developed and presented. The proposed SMART based technique demonstrates a new framework to apply SB based variable substitution for rapid multicoil image reconstruction. Compared to the standard GD based method, the SMART implementation is able to reconstruct images rapidly, with a speedup of ~6. The method has been developed for 2D multislice DCE cardiac perfusion images, though the SMART method is applicable to 3D+time acquisition methods or any other type of accelerated data acquisitions that use L_1 norm based reconstruction methods to drive sparsity. Further investigation is needed to build on these initial results which show that the new SMART based method is a promising approach to reconstruct multicoil images rapidly.

ACKNOWLEDGMENTS

This work is supported by No. R01HL113224. The authors thank the anonymous reviewers whose suggestions helped greatly to improve the paper.

APPENDIX: COMPARISON OF RAPID MULTICOIL RECONSTRUCTION TECHNIQUES

SB is a popular technique which has been used to accelerate TV based image denoising[11] and image restoration.[33] The principle of SB-based variable substitution is also useful at

accelerating single coil MR reconstructions. For example, in Ref. 34, a SB-based technique is used to accelerate reconstruction of cine images. A spatiotemporal TV constraint combined with a motion compensation technique that uses a free-form deformation (FFD) model is used to mitigate the effects of motion in the acquired data. The formulation is then minimized with a combination of soft-thresholding and a biconjugated gradient stabilized (BiCGSTAB) method. The focus of this paper is on developing a rapid minimization technique for TV based multicoil reconstructions. Hence the comparisons made in the Appendix are limited to techniques that have been developed to accelerate sparse-SENSE type reconstructions.

1. Existing methods for accelerating multicoil reconstructions

In order to put the methods proposed here in context, we examine published methods for minimizing the constrained sparse-SENSE cost functional given in Eq. (1). In this section, the approaches from six groups that have proposed methods for rapidly minimizing Eq. (1) or a similar cost functional are summarized.

a. Method developed by Bilen et al.

In Ref. 35, temporal TV and temporal wavelets are used as sparsifying constraints φ_1 and φ_2. A version of FISTA (Refs. 35 and 36) is used to minimize the cost functional. This method has been tested on retrospectively undersampled cardiac perfusion data. Though the method is tested only with temporal constraints, spatial TV constraints can also be included in this framework.

b. Variable splitting based method developed by Ye et al.

In Ref. 37, TV and wavelets applied along the spatial dimension are used as sparsifying constraints φ_1 and φ_2. To accelerate reconstruction, an auxiliary variable is used to decouple the image term from the sparsity constraints by adding an L_2 norm squared penalty between the new auxiliary variable and the image term. By using this variable splitting step, the minimization problem is reduced to a combination of a least squares problem and an L_1 norm denoising/filtering problem.

Using the method developed in Ref. 37, by enforcing $m = v$, where v is the auxiliary variable, Eq. (1) can be rewritten as

$$\underset{m}{\operatorname{argmin}} \frac{\alpha}{2}\|m-v\|_2^2+\frac{\mu}{2}\sum_{i=1}^{N\text{Coils}}\|EC_im-k_i\|_2^2, \tag{A1}$$

$$\underset{v}{\operatorname{argmin}} \|\varphi_1 v\|_1+\|\varphi_2 v\|_1+\frac{\alpha}{2}\|v-m\|_2^2. \tag{A2}$$

Equation (A2) is minimized in Ref. 37 by using the SB approach of variable substitution followed by soft-thresholding, while Eq. (A1) is minimized using the iterative reweighting scheme used in FISTA.[37] The method has been tested on retrospectively undersampled brain data. Though not used in Ref. 37, the variable splitting could have been performed by using a SB-based formulation, instead of using an L_2 norm squared based penalty. Unlike SMART, this method does not make a surrogate variable based substitution for C_im. The surrogate variable based substitution $m = v$ is made using a least squared constraint and not AL/SB.

c. Proximal operator based method developed by Montefusco et al.

An alternate approach is developed in Ref. 18 for fast reconstruction of 3D MR images. This approach is based on the use of a proximal operator to make the reconstruction problem in Eq. (1) easier to minimize using the following steps:

$$v = \underset{m}{\operatorname{argmin}} \sum_{i=1}^{N\text{Coils}}\|EC_im-k_i\|_2^2. \tag{A3}$$

The update step is given by

$$v^n = m^n+\alpha\sum_{i=1}^{N\text{Coils}}(EC_i)^{*T}(k_i-EC_im), \tag{A4}$$

$$m^{n+1} = \underset{m}{\operatorname{argmin}} \|\varphi m\|_1+\frac{\mu}{2\alpha}\|m-v^n\|_2^2. \tag{A5}$$

Here the sparsity constraint φ is composed of gradients applied in 3D, using an 18-neighbor structure to calculate the gradients. $*T$ is the conjugate-transpose operator. Equation (A5) is minimized using a recursive median filter.[18] A FISTA-based iterative reweighting scheme is used to accelerate convergence. That is, here no substitution is made to C_im and the constraints are applied to a 3D block, unlike SMART, which is designed to handle constraints along the spatial and temporal dimensions separately.

d. Fast composite splitting algorithm (FCSA) based method developed by Jiang et al.

A third group developed a fast minimization algorithm[38] by using a composite splitting method.[39] The reconstruction method in Ref. 38 has two sparsity constraints like the variable splitting method in Ref. 37, but uses FCSA to reduce Eq. (1) to a combination of two simpler subproblems,

$$\underset{m}{\operatorname{argmin}} \|\varphi_1 m\|_1+\frac{\mu}{2}\sum_{i=1}^{N\text{Coils}}\|EC_im-k_i\|_2^2, \tag{A6}$$

$$\underset{m}{\operatorname{argmin}} \|\varphi_2 m\|_1+\frac{\mu}{2}\sum_{i=1}^{N\text{Coils}}\|EC_im-k_i\|_2^2. \tag{A7}$$

In Ref. 38, φ_1 and φ_2 are spatial gradients and spatial wavelets, respectively. Equations (A6) and (A7) are individually minimized using FISTA and the final solution is computed using a linear combination of the solution of the two subproblems (A6) and (A7). Although this method uses spatial constraints, the framework can easily be extended to include temporal constraints.

The methods mentioned above either do not utilize the SB/AL framework or do not utilize it completely, likely reducing the efficiency of these fast minimization techniques. These methods do not make any substitutions to the fidelity constraint term, which is unlike the methods discussed below which utilize the SB/AL framework to accelerate convergence.

e. SB/AL based methods

Methods have been developed based on the SB/AL framework in Refs. 15 and 14. In Ref. 14, multiple auxiliary variables are used in a SB/AL framework (named as P2 in Ref. 14) with the following substitutions: $x = m$, $P_i = C_i m$, and $v = \varphi x$,

$$\begin{aligned}\underset{m,P,\hat{P},v,\hat{v},x,\hat{x}}{\operatorname{argmin}} &\|v\|_1 + \frac{\mu}{2}\sum_{i=1}^{N\text{Coils}} \|EP_i - k_i\|_2^2 \\ &+ \frac{\alpha_1}{2}\left\|P_i - C_i m - \hat{P}_i\right\|_2^2 + \frac{\alpha_2}{2}\|x - m - \hat{x}\|_2^2 \\ &+ \frac{\alpha_3}{2}\|v - \varphi x - \hat{v}\|_2^2. \end{aligned} \tag{A8}$$

Efficient closed-form solutions were developed for computing terms such as $\left(\alpha_2 I + \alpha_3 \varphi^T \varphi\right)^{-1}$, $\left(\alpha_2 I + \alpha_1 C^T C\right)^{-1}$, and $\left(\alpha_1 I + \mu E^T E\right)^{-1}$. The method has been tested on retrospectively undersampled MRI brain data using a Poisson-disk based sampling pattern. The method is developed only for reconstruction problems that use spatial constraints and will need to be extended and tested for dynamic data, where utilizing correlations in time is necessary.

The method developed in Ref. 15 to minimize Eq. (1) uses fewer substitutions compared to Ref. 14. The steps are as follows:

Enforcing $x = m$ and $v = \varphi x$ to Eq. (1) using SB,

$$\begin{aligned}\underset{m,v,\hat{v},x,\hat{x}}{\operatorname{argmin}} &\|v\|_1 + \frac{\mu}{2}\sum_{i=1}^{N\text{Coils}} \|EC_i m - k_i\|_2^2 \\ &+ \frac{\alpha_1}{2}\|v - \varphi x - \hat{v}\|_2^2 + \frac{\alpha_2}{2}\|x - m - \hat{x}\|_2^2. \end{aligned} \tag{A9}$$

Minimization of Eq. (A9) involves computing $(\alpha_2 I + \mu(EC)^T EC)^{-1}$ and $\left(\alpha_2 I + \alpha_1 \varphi^T \varphi\right)^{-1}$. Methods based on the use of singular value decomposition (SVD) have been developed to quickly compute $\left(\alpha_2 I + \mu(EC)^T EC\right)^{-1}$. When constraints such as wavelet transform or Fourier transforms are used for φ, efficient closed-form solutions are available for computing $\left(\alpha_2 I + \alpha_1 \varphi^T \varphi\right)^{-1}$, whereas CG can be used for constraints such as temporal TV.[15] A similar algorithm was also developed for synthesis prior based reconstruction.[15] The method has been tested on retrospectively undersampled cardiac data, undersampled with a variable density undersampling pattern. It is to be noted that the method was developed only for Cartesian sampled data. For data acquired on non-Cartesian grid points, the method would have to be modified. The speed of this algorithm depends on how quickly the matrix inverses can be calculated. Efficient methods have been developed for Cartesian sampled data, though for radial data, conjugate gradient type methods would have to be used.

f. SMART formulation

Start from Eq. (1), given by

$$\underset{m}{\operatorname{argmin}}\, \lambda_1\|\varphi_1 m\|_1 + \lambda_2\|\varphi_2 m\|_1 + \frac{\mu}{2}\sum_{i=1}^{N\text{Coils}} \|EC_i m - k_i\|_2^2. \tag{1}$$

The SMART formulation makes the following substitutions: $P_i = C_i m$, $v_1 = \varphi_1 m$, and $v_2 = \varphi_2 m$. Enforcing the variable substitutions using SB, Eq. (1) can be rewritten as

$$\begin{aligned}\underset{m}{\operatorname{argmin}}\, &\lambda_1\|v_1\|_1 + \lambda_2\|v_2\|_1 + \frac{\mu}{2}\sum_{i=1}^{N\text{Coils}} \|EP_i - k_i\|_2^2 \\ &+ \frac{\alpha_1}{2}\|v_1 - \varphi_1 m - \hat{v}_1\|_2^2 + \frac{\alpha_2}{2}\|v_2 - \varphi_2 m - \hat{v}_2\|_2^2 \\ &+ \frac{\beta}{2}\sum_{i=1}^{N\text{Coils}} \left\|P_i - C_i m - \hat{P}_i\right\|_2^2. \end{aligned} \tag{A10}$$

A comparison of Eq. (A10) [or Eq. (3)] with Eqs. (A8) and (A9) shows that the SB based formulation developed here is different from the SB/AL based formulation developed in Ref. 14 [Eq. (A8)] and Ref. 15 [Eq. (A9)]. Unlike Ref. 14, the SMART implementation does not use a surrogate variable to approximate m and does not require methods to invert large matrices such as those used in Refs. 14 and 15.

The SMART method uses few SB based variable substitutions and is compatible with both Cartesian and radial data. The implementation of SMART does not require inversion of large matrices.

[a]Author to whom correspondence should be addressed. Electronic mail: edward.dibella@hsc.utah.edu

[1]K. P. Pruessmann, M. Weiger, M. B. Scheidegger, and P. Boesiger, "SENSE: Sensitivity encoding for fast MRI," Magn. Reson. Med. **42**, 952–962 (1999).
[2]M. A. Griswold, P. M. Jakob, R. M. Heidemann, M. Nittka, V. Jellus, J. Wang, B. Kiefer, and A. Haase, "Generalized autocalibrating partially parallel acquisitions (GRAPPA)," Magn. Reson. Med. **47**, 1202–1210 (2002).
[3]Z. Yihang, C. Yuchou, L. Dong, and L. Ying, Presented at the 9th IEEE International Symposium on Biomedical Imaging (ISBI), 2012.
[4]Y. Chang, D. Liang, and L. Ying, "Nonlinear GRAPPA: A kernel approach to parallel MRI reconstruction," Magn. Reson. Med. **68**, 730–740 (2012).
[5]K. T. Block, M. Uecker, and J. Frahm, "Undersampled radial MRI with multiple coils. Iterative image reconstruction using a total variation constraint," Magn. Reson. Med. **57**, 1086–1098 (2007).
[6]L. Ying, B. Liu, M. C. Steckner, G. Wu, M. Wu, and S.-J. Li, "A statistical approach to SENSE regularization with arbitrary k-space trajectories," Magn. Reson. Med. **60**, 414–421 (2008).
[7]R. Otazo, D. Kim, L. Axel, and D. K. Sodickson, "Combination of compressed sensing and parallel imaging for highly accelerated first-pass cardiac perfusion MRI," Magn. Reson. Med. **64**, 767–776 (2010).
[8]L. Feng, R. Grimm, K. T. Block, H. Chandarana, S. Kim, J. Xu, L. Axel, D. K. Sodickson, and R. Otazo, "Golden-angle radial sparse parallel MRI: Combination of compressed sensing, parallel imaging, and golden-angle radial sampling for fast and flexible dynamic volumetric MRI," Magn. Reson. Med. **72**, 707–717 (2014).
[9]G. Adluru and E. V. DiBella, "Reconstruction with diffeomorphic motion compensation for undersampled dynamic MRI," Proc. SPIE **8858**, Wavelets and Sparsity XV, 88581X (September 26, 2013).
[10]A. Beck and M. Teboulle, "A fast iterative shrinkage-thresholding algorithm for linear inverse problems," SIAM J. Imaging Sci. **2**, 183–202 (2009).
[11]T. Goldstein and S. Osher, "The split Bregman method for L1-regularized problems," SIAM J. Imaging Sci. **2**, 323–343 (2009).
[12]C. Wu and X. Tai, "Augmented Lagrangian method, dual methods, and split Bregman iteration for ROF, vectorial TV, and high order models," SIAM J. Imaging Sci. **3**, 300–339 (2010).

[13]P. Combettes and V. Wajs, "Signal recovery by proximal forward-backward splitting," Multiscale Model. Simul. **4**, 1168–1200 (2005).
[14]S. Ramani and J. A. Fessler, "Parallel MR image reconstruction using augmented Lagrangian methods," IEEE Trans. Med. Imaging **30**, 694–706 (2011).
[15]C. Bilen, Y. Wang, and I. W. Selesnick, "High-speed compressed sensing reconstruction in dynamic parallel MRI using augmented Lagrangian and parallel processing," IEEE J. Emerging Sel. Top. Circuits Syst. **2**, 370–379 (2012).
[16]S. Bagchi and S. K. Mitra, *The Nonuniform Discrete Fourier Transform and its Applications in Signal Processing* (Kluwer Academic, Norwell, MA, 1999).
[17]G. Adluru, R. T. Whitaker, and E. V. DiBella, Presented at the 4th IEEE International Symposium on Biomedical Imaging: From Nano to Macro (ISBI), 2007.
[18]L. B. Montefusco, D. Lazzaro, S. Papi, and C. Guerrini, "A fast compressed sensing approach to 3D MR image reconstruction," IEEE Trans. Med. Imaging **30**, 1064–1075 (2011).
[19]G. Adluru and E. DiBella, "Compression^2: Compressed sensing with compressed coil arrays," J. Cardiovasc. Magn. Reson. **14**, 1–2 (2012).
[20]T. Zhang, J. M. Pauly, S. S. Vasanawala, and M. Lustig, "Coil compression for accelerated imaging with Cartesian sampling," Magn. Reson. Med. **69**, 571–582 (2013).
[21]G. Adluru, C. McGann, P. Speier, E. G. Kholmovski, A. Shaaban, and E. V. R. DiBella, "Acquisition and reconstruction of undersampled radial data for myocardial perfusion magnetic resonance imaging," J. Magn. Reson. Imaging **29**, 466–473 (2009).
[22]D. O. Walsh, A. F. Gmitro, and M. W. Marcellin, "Adaptive reconstruction of phased array MR imagery," Magn. Reson. Med. **43**, 682–690 (2000).
[23]D. Likhite, G. Adluru, N. Hu, C. McGann, and E. DiBella, "Quantification of myocardial perfusion with self-gated cardiovascular magnetic resonance," J. Cardiovasc. Magn. Reson. **17**, 1–15 (2015).
[24]S. G. Lingala, E. DiBella, G. Adluru, C. McGann, and M. Jacob, "Accelerating free breathing myocardial perfusion MRI using multi coil radial k-t SLR," Phys. Med. Biol. **58**, 7309–7327 (2013).
[25]T. D. F. Crete, P. Ladret, and M. Nicolas, "The blur effect: Perception and estimation with a new no-reference perceptual blur metric," Proc. SPIE **6492**, 64920I (2007).
[26]A. Harrison, G. Adluru, K. Damal, A. M. Shaaban, B. Wilson, D. Kim, C. McGann, N. F. Marrouche, and E. DiBella, "Rapid ungated myocardial perfusion cardiovascular magnetic resonance: Preliminary diagnostic accuracy," J. Cardiovasc. Magn. Reson. **15**, 26 (2013).
[27]X.-C. Tai and C. Wu, "Augmented Lagrangian method, dual methods and split Bregman iteration for ROF model," in *Scale Space and Variational Methods in Computer Vision*, edited by X.-C. Tai, K. Mørken, M. Lysaker, and K.-A. Lie (Springer, Berlin, Heidelberg, 2009), Vol. 5567, pp. 502–513.
[28]S. G. Lingala, E. DiBella, and M. Jacob, "Deformation corrected compressed sensing (DC-CS): A novel framework for accelerated dynamic MRI," IEEE Trans. Med. Imaging **34**, 72–85 (2015).
[29]X. Chen, M. Salerno, Y. Yang, and F. H. Epstein, "Motion-compensated compressed sensing for dynamic contrast-enhanced MRI using regional spatiotemporal sparsity and region tracking: Block low-rank sparsity with motion-guidance (BLOSM)," Magn. Reson. Med. **72**, 1028–1038 (2014).
[30]M. Usman, D. Atkinson, F. Odille, C. Kolbitsch, G. Vaillant, T. Schaeffter, P. G. Batchelor, and C. Prieto, "Motion corrected compressed sensing for free-breathing dynamic cardiac MRI," Magn. Reson. Med. **70**, 504–516 (2013).
[31]D. M. Strong, P. Blomgren, and T. F. Chan, "Spatially adaptive local-feature-driven total variation minimizing image restoration," Proc. SPIE **3167**, Statistical and Stochastic Methods in Image Processing II, 222 (October 14, 1997).
[32]S. K. Iyer, T. Tasdizen, and E. DiBella, "Edge-enhanced spatiotemporal constrained reconstruction of undersampled dynamic contrast-enhanced radial MRI," Magn. Reson. Imaging **30**, 610–619 (2012).
[33]S. Osher, M. Burger, D. Goldfarb, J. Xu, and W. Yin, "An iterative regularization method for total variation-based image restoration," Multiscale Model. Simul. **4**, 460–489 (2005).
[34]J. F. P. J. Abascal, P. Montesinos, E. Marinetto, J. Pascau, and M. Desco, "Comparison of total variation with a motion estimation based compressed sensing approach for self-gated cardiac cine MRI in small animal studies," PLoS One **9**, e110594 (2014).
[35]C. Bilen, I. W. Selesnick, Y. Wang, R. Otazo, D. Kim, L. Axel, and D. K. Sodickson, "On compressed sensing in parallel MRI of cardiac perfusion using temporal wavelet and TV regularization," in *IEEE International Conference on Acoustics Speech and Signal Processing (ICASSP), Dallas, TX* (IEEE, 2010), pp. 630–633.
[36]A. Beck and M. Teboulle, "Fast gradient-based algorithms for constrained total variation image denoising and deblurring problems," IEEE Trans. Image Process. **18**, 2419–2434 (2009).
[37]X. Ye, Y. Chen, W. Lin, and F. Huang, "Fast MR image reconstruction for partially parallel imaging with arbitrary k space trajectories," IEEE Trans. Med. Imaging **30**, 575–585 (2011).
[38]M. Jiang, J. Jin, F. Liu, Y. Yu, L. Xia, Y. Wang, and S. Crozier, "Sparsity-constrained SENSE reconstruction: An efficient implementation using a fast composite splitting algorithm," Magn. Reson. Imaging **31**, 1218–1227 (2013).
[39]J. Huang, S. Zhang, and D. N. Metaxas, "Efficient MR image reconstruction for compressed MR imaging," Med. Image Anal. **15**(5), 670–679 (2011).

CHAPTER 5

A COMPARISON OF SPLIT BREGMAN AND AUGMENTED LAGRANGIAN METHODS

5.1 Split Bregman and augmented Lagrangian methods

The following derivation demonstrates the equivalence between SB and AL methods by showing that both of the methods are minimizing the same optimality condition when certain conditions are met.

5.1.1 Split Bregman (SB)

The cost functional used in Chapter 3 minimizes the constrained version of the SB formulation, given by

$$C_1 = \underset{\arg\min m}{} \left\| \phi m \right\|_1 + \frac{\mu}{2} \left\| Em - k^i \right\|_2^2 \tag{5.1}$$

$$k^{i+1} = k^i + k^0 - Em^{i+1}. \tag{5.2}$$

Here ϕ is the sparsifying transform, E the data encoding matrix, m is the image being estimated, and k the measured k-space data. Updating k, as shown in (5.2), is the "adding noise back" term. Here TV is used as the sparsifying transform. Hence (5.1) can be rewritten as

$$C_1 = \underset{\arg\min m}{} \left\| \nabla m \right\|_1 + \frac{\mu}{2} \left\| Em - k^i \right\|_2^2 . \tag{5.3}$$

Enforcing variable substitution to the L_1 norm term using SB we get

$$C_1 = \underset{\arg\min m,d,b}{} \left\| d \right\|_1 + \frac{\mu}{2} \left\| Em - k^i \right\|_2^2 + \frac{\lambda}{2} \left\| d - \nabla m - b \right\|_2^2 . \tag{5.4}$$

Combining terms containing m

$$C_1(m) = \underset{\arg\min m}{} \frac{\mu}{2} \left\| Em - k^i \right\|_2^2 + \frac{\lambda}{2} \left\| d - \nabla m - b \right\|_2^2 + \text{constant} . \tag{5.5}$$

Differentiating (5.5) with regard to m we get the optimality condition

$$\mu E^* (Em - k^i) + \lambda \nabla . (d - \nabla m - b) = 0 \tag{5.6}$$

$$(\mu E^* E - \lambda\Delta)m^{i+1} = (\mu E^* k^i - \lambda\nabla.(d^i - b^i)). \tag{5.7}$$

Here E^* is the complex adjoint of E.

5.1.2 Augmented Lagrangian (AL)

To minimize the constrained version of the optimization problem using AL

$$\arg\min_m \|\nabla m\|_1; S.T.\ Em = k \tag{5.8}$$

$$A = \arg\min_m \|\nabla m\|_1 + \frac{\mu}{2}\|Em - k\|_2^2 + \lambda^i(Em - k). \tag{5.9}$$

Here λ^i are the Lagrangian weights and μ is a constant weight. Using completion of squares on (5.9)

$$A = \arg\min_m \|\nabla m\|_1 + \frac{\mu}{2}\|Em - k\|_2^2 + \lambda^i(Em - k) + \frac{1}{2\mu}\|\lambda^i\|_2^2 - \frac{1}{2\mu}\|\lambda^i\|_2^2 \tag{5.10}$$

$$= \arg\min_m \|\nabla m\|_1 + \frac{\mu}{2}\left\|Em - k + \frac{1}{\mu}\lambda^i\right\|_2^2 - \frac{1}{2\mu}\|\lambda^i\|_2^2. \tag{5.11}$$

Assuming N^i to be of the form

$$N^i = \frac{-1}{\mu}\lambda^i \tag{5.12}$$

$$A = \arg\min_m \|\nabla m\|_1 + \frac{\mu}{2}\|Em - k - N^i\|_2^2 - \frac{1}{2\mu}\|\lambda^i\|_2^2. \tag{5.13}$$

N^i is the "noise" that is updated as

$$N^{i+1} = N^i + (k - Em^{i+1}). \tag{5.14}$$

Assuming

$$k + N^i = k^i \tag{5.15}$$

(5.14) can we written as

$$A=_{\arg\min m}\left\|\nabla m\right\|_1+\frac{\mu}{2}\left\|Em-k^i\right\|_2^2-\frac{1}{2\mu}\left\|\lambda^i\right\|_2^2. \tag{5.16}$$

Comparing (5.16) with (5.3), both the equations have the same objective function up to a constant.

To further minimize (5.16), we enforce variable substitution in the L_1 norm term using AL

$$A(m)=_{\arg\min m}\lambda_1^i(d-\nabla m)+\frac{\mu_1}{2}\left\|d-\nabla m\right\|_2^2+\frac{\mu}{2}\left\|Em-k^i\right\|_2^2+\text{Constant}. \tag{5.17}$$

Differentiating (5.17) with regard to *m* we get the optimality condition

$$\mu E^*(Em-k^i)+\mu_1\nabla.(d-\nabla m)+\nabla.\lambda_1^i=0 \tag{5.18}$$

$$(\mu E^*E-\mu_1\Delta)m^{i+1}=(\mu E^*k^i-\mu_1\nabla.(d^i+\frac{1}{\mu_1}\lambda_1^i)). \tag{5.19}$$

Comparing (5.19) with (5.7), the near equivalence between SB and AL is seen.

If $\mu_1=\lambda$ and $\frac{1}{\mu_1}\lambda_1^i=-b^i$, both SB and AL have the same optimality condition.

CHAPTER 6

CONCLUSION

6.1 Summary of contribution

This research was motivated by the desire to develop better TV reconstruction techniques for reconstructing images from highly undersampled k-space data. Improved TV reconstruction techniques were developed to tackle the issues of poor reconstructed image quality for data acquired at high acceleration factors and slow reconstruction speeds. These improved TV methods were tested on contrast-enhanced cardiac MR images, namely cardiac perfusion images and 3D LGE images of the LA.

Chapter 2 focused on a TV-based reconstruction method for gated cardiac perfusion imaging. The method used spatially varying weights on the spatial TV constraint to prevent smoothing of edges. In addition, an edge-matching term was used to enhance the sharpness of the edges in the reconstructed image. This method was developed to show that instead of using a constant weight on the TV constraint, as is usually used in most TV reconstruction formulations, using a data-dependent reference image to vary the weights on the TV constraints helps prevent smoothing of edges. The reconstructed images had a sharper edge profile and better contrast when compared to the images reconstructed by the TV-based reconstruction technique that uses constant weights on TV. A gradient descent-based implementation was used to minimize the cost functionals.

Chapter 3 focused on methods to improve 3D LGE imaging. The aim was to develop a technique to reduce the scan time by heavily undersampling the acquired k-space data, while maintaining high image quality by using a 3D TV constraint. A SB-based approach was used to rapidly minimize the cost functional. This was done to develop a reconstruction technique that could reconstruct images rapidly. The method was tested on retrospectively undersampled preablation and postablation datasets as a preliminary study.

The study showed that it is possible to achieve high acceleration factors (R~3), while maintaining good image quality by the use of a 3D TV constraint and rapid convergence with an SB formulation.

Chapter 4 demonstrated a new technique for rapidly minimizing multicoil reconstructions. A new SB-based variable substitution method was developed. The aim was to develop a fast minimization technique that forms a good balance between the amount of memory used due to variable substitution and reconstruction speed. The method was tested on gated and ungated DCE cardiac perfusion images, and improvements were seen in the reconstruction speed and image quality when compared to a gradient descent-based implementation of the same cost functional.

Chapter 5 provided a comparison of the SB and AL techniques and showed how the adding noise back step that is often used with SB can also be derived using AL.

6.2 Future work

The reconstruction method in Chapter 2 made the weights on the spatial TV constraint spatially varying. As part of future study, the idea could be extended along the temporal dimension, making the weights on the temporal TV constraint temporally varying. Another improvement could be the use of a multicoil version of the proposed method, instead of a coil-by-coil reconstruction technique. A multicoil reference image could be generated to extract the edge information as opposed to generating a different reference image for each coil data.

The multicoil reconstruction formulation discussed in Chapter 4 uses TV constraints along the spatial and temporal dimensions. There are good correlations along

the slice dimension, and constraints could be applied to slice dimension to improve image quality. The existing SMART framework allows for these improvements to be tested without the necessity for any major modification to the minimization algorithm.

The techniques in this dissertation try to address some of the challenges facing reconstruction of DCE cardiac MR imaging. I envision a day when CS-based techniques become a mature technology and are widely used by clinicians. Slow reconstruction speed and variability in image quality are some of the challenges that currently do not permit widespread use of CS by clinicians. Techniques developed in this dissertation for rapid and high-quality reconstruction of undersampled DCE MRI images should help in moving in the direction of transitioning CS to a powerful and robust tool that is used routinely by clinicians.